mathematics

Article

Grey-Wolf-Optimization-Algorithm-Based Tuned P-PI Cascade Controller for Dual-Ball-Screw Feed Drive Systems

Qi Liu [1,2], Hong Lu [1,*], Heisei Yonezawa [3], Ansei Yonezawa [3], Itsuro Kajiwara [3] and Ben Wang [1]

[1] School of Mechanical and Electronic Engineering, Wuhan University of Technology, Wuhan 430070, China; liunuli@whut.edu.cn (Q.L.); wangben1234@whut.edu.cn (B.W.)
[2] Division of Human Mechanical Systems and Design, Hokkaido University, N13, W8, Kita-ku, Sapporo 060-8628, Hokkaido, Japan
[3] Division of Mechanical and Aerospace Engineering, Hokkaido University, N13, W8, Kita-ku, Sapporo 060-8628, Hokkaido, Japan; yonezawah@eng.hokudai.ac.jp (H.Y.); ayonezawa@eng.hokudai.ac.jp (A.Y.); ikajiwara@eng.hokudai.ac.jp (I.K.)
* Correspondence: landzh@whut.edu.cn

Abstract: Dual-ball-screw feed drive systems (DBSFDSs) are designed for most high-end manufacturing equipment. However, the mismatch between the dynamic characteristic parameters (e.g., stiffness and inertia) and the P-PI cascade control method reduces the accuracy of the DBSFDSs owing to the structural characteristic changes in the motion. Moreover, the parameters of the P-PI cascade controller of the DBSFDSs are always the same even though the two axes have different dynamic characteristics, and it is difficult to tune two-axis parameters simultaneously. A new application of the combination of the grey wolf optimization (GWO) algorithm and the P-PI cascade controller is presented to solve these problems and enhance the motion performance of DBSFDSs. The novelty is that the flexible coupling model and dynamic stiffness obtained from the motor current can better represent the two-axis coupling dynamic characteristics, and the GWO algorithm is used to adjust the P-PI controller parameters to address variations in the positions of the moving parts and reflect characteristic differences between the two axes. Comparison of simulation and experimental results validated the superiority of the proposed controller over existing ones in practical applications, showing a decrease in the tracking error of the tool center and non-synchronization error of over 34% and 39%, respectively.

Keywords: grey wolf optimization algorithm; P-PI cascade controller; dual-ball-screw feed drive system; dynamic characteristic parameter; characteristic variation; flexible coupling model

MSC: 93C95

check for updates

Citation: Liu, Q.; Lu, H.; Yonezawa, H.; Yonezawa, A.; Kajiwara, I.; Wang, B. Grey-Wolf-Optimization-Algorithm-Based Tuned P-PI Cascade Controller for Dual-Ball-Screw Feed Drive Systems. *Mathematics* **2023**, *11*, 2259. https://doi.org/10.3390/math11102259

Academic Editor: Ioannis G. Tsoulos

Received: 11 April 2023
Revised: 8 May 2023
Accepted: 10 May 2023
Published: 11 May 2023

1. Introduction

1.1. Background of the Research

Motion inaccuracy has been a limiting factor in high-precision machining in several industries for decades. The mismatch between servo control and dynamic characteristic parameters of feed drive systems (FDSs) is one of the reasons for this inaccuracy [1,2]. The proportional-integral-derivative (PID) control method is most commonly used in industrial control systems as a standard effective solution [3–5]. During operation, the structure of the FDS is time varying, which will change the dynamic characteristic parameters such as the transmission stiffness and rotational inertia, and cause serious vibrations [6]. Even though the dynamic characteristic parameters of the FDS are variable, the conventional PID control method has constant parameters that cannot maintain a better performance during motion [7,8].

Dual-ball-screw feed drive systems (DBSFDSs), as an innovative structure, have been widely implemented in high-end industrial applications, for example, precision CNC equipment, owing to their high transmission stiffness, quick responsiveness, and high driving forces [9,10]. The two ball-screw FDSs in a DBSFDS were adopted to drive the crossbeam or worktable based on the principle of Driving at the Center of Gravity (DCG), as shown in position B of Figure 1c. Figure 1a shows the usage examples of a DBSFDS, and Figure 1b shows the general structure of a DBSFDS. The crossbeam, which moves along the X1-axis and X2-axis, is driven by a mechanical system containing two FDSs consisting of dual servo motors, dual ball screws, dual linear guides, and bearings. The crossbeam serves as the base of the Y-axis motor carrying the moving parts. The moving parts can be moved with a tool or any other device. However, the movement of the moving parts causes the loads on the X1-axis and X2-axis to be different. This variation makes it difficult to directly employ the principle of DCG in the moving process, as shown in position A of Figure 1d. Furthermore, the structural characteristic changes result in different dynamic characteristics of the two axes [11].

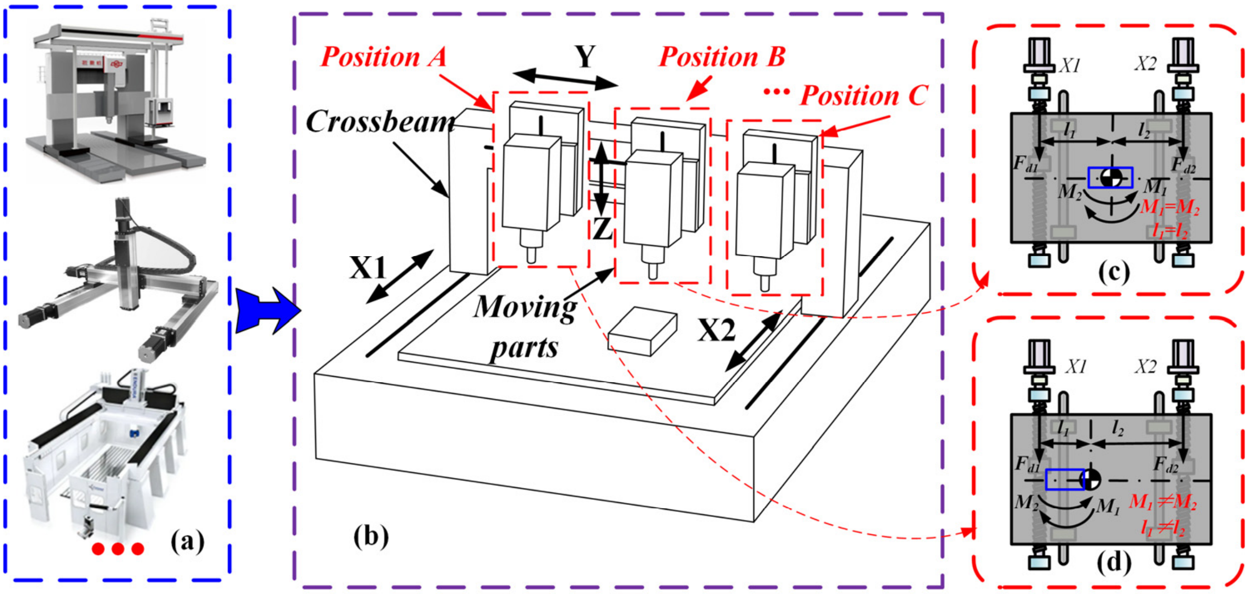

Figure 1. The general structure of a DBSFDS. (**a**) Machine tool using a DBSFDS. (**b**) Structure of the DBSFDSs. (**c**) Obedience to the principle of DCG. (**d**) Disobedience to the principle of DCG.

The center of gravity is shifted due to the variable position of the moving parts along the crossbeam and the difference in mechanical characteristics between the two axes induces non-synchronous errors, resulting in the ‘push-and-drag’ phenomenon. Ultimately, the accuracy of the tool center is destroyed [12]. As shown in Figure 2, the non-synchronous error refers to the different motion accuracies of the X1-axis FDS and X2-axis FDS. Four types of non-synchronous situations occur during the motion in Figure 2, and the accuracy of the tool center is affected by the positions of the moving parts and the coupling characteristics of the X1-axis and X2-axis FDSs.

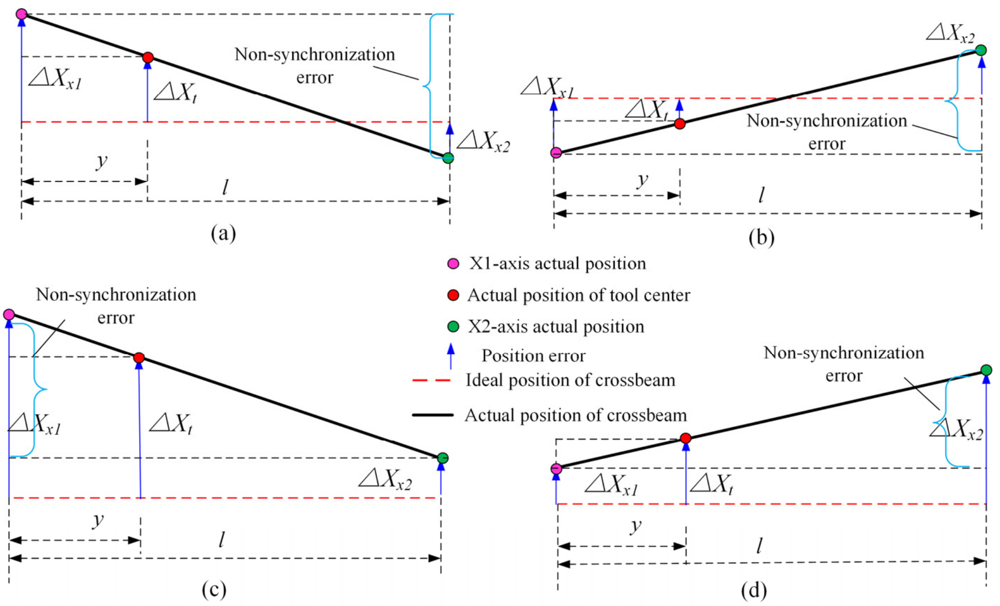

Figure 2. Non-synchronous situations of DBSFDSs. (**a**) Non-synchronous situation 1#. (**b**) Non-synchronous situation 2#. (**c**) Non-synchronous situation 3#. (**d**) Non-synchronous situation 4#.

The relationship between the X1- and X2-axis position errors and the tool center position error can be obtained using Equation (1), where y indicates the position of the moving parts and its expression is $y = \int v_y dt$, where v_y is the velocity of moving parts, l is the length of the crossbeam, and x_0, x_1, and x_2 refer to the motion instruction, X1-axis actual position, and X2-axis actual position, respectively. ΔX_t, ΔX_{x1}, and ΔX_{x2} are the position errors of the tool center, X1-axis, and X2-axis, respectively. $\min(x_1, x_2) < x_0$ represents the nonsynchronous situations shown in Figure 2a,b. $\min(x_1, x_2) > x_0$ indicates the nonsynchronous situations in Figure 2c,d. According to Equation (1), the position error of the tool center is influenced by the positions of the moving parts and by reducing the two-axis error, the tool center accuracy can be improved.

$$\begin{cases} \Delta X_t = \frac{l-y}{l}|x_0 - x_1| - \frac{y}{l}|x_0 - x_2|, \min(x_1, x_2) < x_0 \\ \Delta X_t = \frac{l-y}{l}|x_0 - x_1| + \frac{y}{l}|x_0 - x_2|, \min(x_1, x_2) > x_0 \end{cases} \tag{1}$$

As two FDSs are coupled to each other by the crossbeam during motion, the dynamic characteristics change with the variation in the position of the moving parts, as shown in Figures 1 and 2, thus affecting the motion accuracy of the DBSFDSs. Excessive non-synchronous errors cause the crossbeam to twist and compress the ball screw and guide rail, which determines the machining accuracy of the machine tool. In traditional PID control, once the parameters of the controller are determined, they are fixed even if the motion state changes or external interference occurs; thus, the performance of the controller cannot be guaranteed [13]. Therefore, improving the precision of PID control for DBSFDSs is of great significance. In addition, how to reduce the effect of the two-axis error on the tool center error in DBSFDSs in the process of parameter adjustment poses a challenge to the PID-parameter adjustment of CNC equipment using DBSFDSs.

1.2. Related Work

There are two types of PID tuning methods for FDS: the empirical trial-and-error method and the use of metaheuristic algorithms for tuning [14–16]. As the representative of empirical trial-and-error method, the Ziegler–Nichols (ZN) method is commonly used in industrial applications. The ZN method provides a simple way to reflect dynamic characterization in terms of system responses and is used as a classical tuning criterion of the empirical trial-and-error method [17,18]. However, there are some drawbacks to the ZN method, which include excessive aggressiveness for many industrial control systems and poor robustness in the design of closed-loop systems [19,20]. Additionally, the ZN method cannot always provide a truly optimal solution. This is because the tuning process depends on the manual tuning. Using empirical trial-and-error methods to adjust the PID parameters for DBSFDSs makes it difficult to obtain good accuracy in the movement of DBSFDSs. This is because the PID parameters for both FDSs cannot be adjusted simultaneously.

The metaheuristic algorithms can be classified as nature-inspired algorithms and non-nature-inspired algorithms [21]. The nature-inspired algorithms have been widely studied and developed, which can be generally classified as evolutionary, swarm intelligence, and physics-based algorithms. Evolutionary algorithms are represented by the Genetic Algorithm (GA) [22], differential evolution algorithm [23], etc., while the swarm intelligence algorithms are represented by the Particle Swarm Optimization (PSO) algorithm [24], Grey Wolf Optimization (GWO) algorithm [25], etc. Water wave optimization [26] and heat transfer search [27] are included in the physics-based algorithms. Table 1 shows the classification, application areas, and properties of the nature-inspired algorithms.

Table 1. The classification of the nature-inspired algorithms.

Classification	Examples	Applications (Not Limited to These Applications)	Properties
Evolutionary algorithms	GA [22], differential evolution algorithm [23]	Parameter optimization of mechanical arm [22], crane systems controlling [23], etc.	Mimic evolutionary phenomena
Swarm intelligence algorithms	PSO algorithm [24], GWO algorithm [25]	PID parameters tuning [24,25], etc.	Imitation of creatures' collective behavior
Physics-based algorithms	Water wave optimization [26], heat transfer search [27]	High-speed train scheduling problem [26], etc.	Obedience to physical laws

Some metaheuristic algorithms used to adjust the PID parameters include Adaptive Fuzzy Logic Controller (AFLC) [28], GA [22], Natural Annealing Particle Swarm Optimization (NAPSO) [24], adaptive particle swarm optimization (APSO) [29], etc. When using an algorithm to tune PID parameters, a physical model of the controlled object needs to be created. A ball screw is used as the drive unit in the FDS, which has flexible characteristics during motion. The axial stiffness of the FDS is usually characterized by theoretical calculation methods or using Experimental Modal Analysis (EMA) in the course of model establishment, but there are theoretical calculation errors owing to the uncertainty of parameter values, and the difference between the static stiffness and the dynamic stiffness under motion will cause a degradation of the control performance [30,31]. Most studies do not consider the dynamic influence of axial stiffness in the process of PID-parameter tuning, which leads to a deviation from the real state and eventually reduces the motion accuracy of the FDS [32].

Reference [33] summarizes that many setting parameters in the GA need to be adjusted, resulting in time consumption with more overshoot and difficulties in programming. The PSO algorithm usually fails to discover the global optimum solution, and it shows poor-quality results with regard to complex and large data sets [34]. In view of the group hunting mechanism and leadership hierarchy of grey wolves, the GWO algorithm is convenient, flexible, and scalable when used and requires no derivation information during the initial search [25]. The GWO algorithm has been generally used in engineering and medical fields to address optimization problems [5]. Some researchers have demonstrated that in the optimization of PID-controller parameters for the motor, the GWO algorithm performs better than the ZN, PSO, and Artificial Bee Colony methods [35–37], because of GWO's accuracy calculation and the smaller population in searching procedures. Due to the advantages of the GWO algorithm, a large number of scholars have studied the GWO algorithm and improved it, such as the adaptive GWO (AGWO) algorithm [38], improved

GWO (IGWO) algorithm [21], and gaze-cues-learning-based grey wolf optimizer (GGWO) algorithm [39]. A feature comparison of the GWO algorithm with other algorithms is shown in Table 2.

Table 2. Comparison of GWO algorithms' characteristics.

Algorithm Name	Features	Applications (Not Limited to These Applications)
GWO [25]	Easy to program, few parameters to set, the operability of the position updating equation	Designing and tuning controllers, robotics, path planning [25], etc.
AGWO [38]	Using fitness-based convergence criteria and introducing a threshold	Optimization problems in science and industry [38], etc.
IGWO [21]	Using dimension learning-based hunting (DLH) search strategy	Engineering problems, e.g., the welded beam design [21], etc.
GGWO [39]	Combining search strategies: neighbor gaze cues learning (NGCL) and random gaze cues learning (RGCL)	Constrained design problems, e.g., tension/compression spring design problem [39], etc.

To solve the mismatch between PID servo control and dynamic characteristic parameters of FDS owing to the crossbeam position variation of DBSFDSs, the GWO algorithm is used to tune the P-PI cascade controller for controlling DBSFDSs, which requires very few parameters to be adjusted. This feature of the GWO algorithm is well suited to solving practical problems of industrial parameter optimization. In order to reduce the influence of the PID parameter regulation due to dynamic stiffness, the axial stiffness of DBSFDSs was considered in the process of PID-parameter adjustment. This paper proposes adopting the motor current to identify the axial stiffness of DBSFDSs, to better reflect the flexible characteristics of DBSFDSs, and provide an accurate model for the proposed control method. The novelties of this study are as follows.

(1) The establishment of a two-axis, flexible coupling model and the use of an innovative approach to identify axial stiffness by motor currents under motion, which does not require additional sensors and can obtain the stiffness of the X1-axis and X2-axis simultaneously.

(2) The GWO algorithm is used to adjust the parameters of the P-PI cascade controller under variations in the positions of the moving parts. This method avoids the problem of not being able to adjust the PID parameters of two FDSs simultaneously considering the different motion characteristics of the two axes, which reduces the impact of structural characteristic changes on the tool center accuracy. Moreover, it can avoid manual trial and error, and multiple parameters of the P-PI controller can be adjusted simultaneously.

(3) The GWO-based tuned P-PI cascade controller is a practical control strategy that is easy to implement in industrial applications compared with cross-coupling control schemes, which are structurally complex and difficult to compute [40]. Experimental verification showed the first application example of the GWO algorithm to adjust the P-PI cascade controller for DBSFDSs, resulting in good control performance.

The rest of the paper is organized as follows. In Section 2, a P-PI cascade controller for DBSFDSs is presented. In Section 3, the flexible coupling model is established, and the adoption of the motor current to identify the axial stiffness in DBSFDSs is presented. The GWO-based tuned P-PI cascade controller is presented in Section 4, and the results and discussion are summarized to validate the benefits of the proposed method in Section 5. This is followed by the conclusion and directions for future work in Section 6.

2. P-PI Cascade Controller for DBSFDSs

Figure 3 shows the typical structure of DBSFDSs; specifically, two ball-screw FDSs collectively drive the gantry-type crossbeam to move. DBSFDSs consist of a servo control system and a mechanical transmission system. The servo control system contains a motion controller, driver, and permanent magnet synchronous motor (PMSM). The mechanical transmission system uses a ball screw and nut, which can achieve high transmission efficiency [41]. A guide rail, slider, and bearing are also used in the FDS.

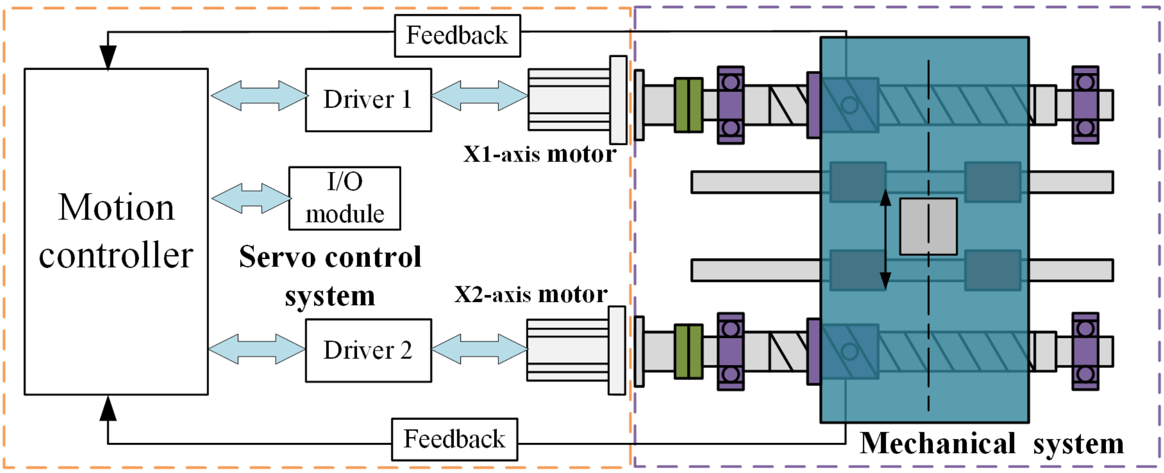

Figure 3. Structure diagram of the DBSFDSs.

Such DBSFDSs are controlled with the aid of P-PI cascade control loops from the inner control loop to the outer control loop, which are operated by a proportional integral (PI) controller, and the position loop is operated by a proportional (P) controller [42]. A mathematical model of the PMSM must be deduced to illustrate the P-PI cascade controller of the DBSFDSs. Figure 4a shows the PMSM structural model. A, B, and C are three stator windings located on the stator, with a difference of 120° between AB, BC, and AC. The d-q coordinate system was set to rotate together on the rotor, and the d-axis was the direction of the excitation flux.

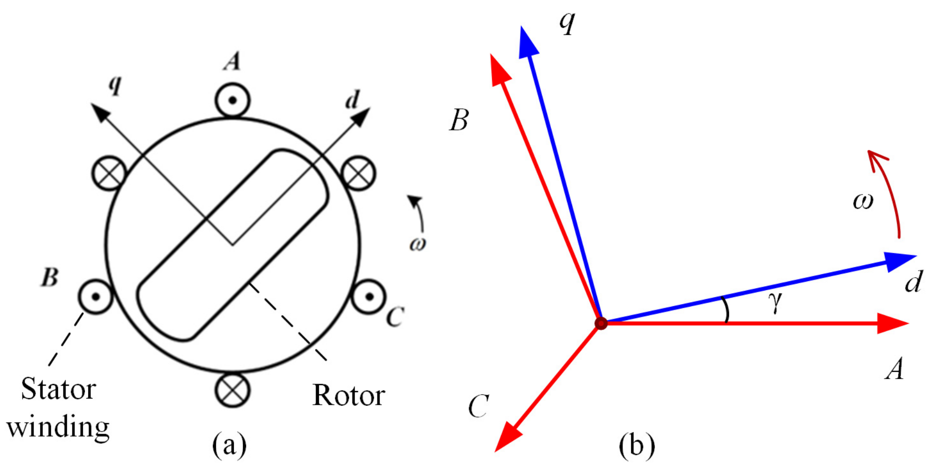

Figure 4. Structure diagram of the PMSM. (**a**) Principal structure and (**b**) coordinate transformation.

The transformation equation for the ABC coordinate system to the d-q coordinate system can be obtained by combining the Clark and Park coordinate transformations. The voltage equation under the ABC coordinate system can be transformed into that under the d-q coordinate system using Equation (2) to obtain a simpler mathematical model of the PMSM, as shown in Figure 4b.

$$C_{dq}^{ABC} = \sqrt{\frac{2}{3}} \begin{bmatrix} \cos\gamma & \cos(\gamma - 120^\circ) & \cos(\gamma + 120^\circ) \\ -\sin\gamma & -\sin(\gamma - 120^\circ) & -\sin(\gamma + 120^\circ) \\ \frac{1}{2} & \frac{1}{2} & \frac{1}{2} \end{bmatrix} \quad (2)$$

According to Equation (2) and the working principle of a three-phase AC-driven PMSM, the voltage equation under the d-q coordinate system for the PMSM can be expressed as [43]

$$\begin{cases} u_d = R_s i_d + \frac{d}{dt}\psi_d - \omega\psi_q \\ u_q = R_s i_q + \frac{d}{dt}\psi_q + \omega\psi_d \end{cases} \tag{3}$$

$$\begin{cases} \psi_d = L_d i_d + \psi_f \\ \psi_q = L_q i_q \end{cases} \tag{4}$$

where ω is the angular velocity of the rotor; R_s is the stator resistance; ψ_d and ψ_q are the magnetic linkages of the d and q axes, respectively; ψ_f indicates the permanent magnet flux vector of the rotor; L_d and L_q refer to the inductance of the d and q axes, respectively; u_d and u_q are the voltages of the d and q axes, respectively; and i_d and i_q are the currents in the d and q axes, respectively.

The electromagnetic torque equation of the PMSM is as follows:

$$\begin{cases} T_e = \frac{3}{2} P_n i_q \left[\psi_f + i_d(L_d - L_q)\right] \\ T_e = J_m \frac{d}{dt}\omega_r + T_d \end{cases} \tag{5}$$

where P_n is the pole pair, J_m is rotational inertia, and $\omega_r = \omega/P_n$. When $L_d = L_q$, Equation (5) can be simplified as follows:

$$\frac{3}{2} P_n i_q \psi_f = J_m \frac{d}{dt}\omega_r + T_d \tag{6}$$

By taking the Laplace transform of Equation (6), Equation (7) can be obtained as:

$$\frac{\omega_r(s)}{K_T I_q(s) - T_d(s)} = \frac{1}{J_m \cdot s} \tag{7}$$

where $\frac{3}{2} P_n \psi_f = K_T$.

If $i_d \equiv 0$, substituting Equation (4) into Equation (3), yields

$$u_q - P_n \omega_r \psi_f = R_s i_q + L_q \frac{d}{dt} i_q \tag{8}$$

By taking the Laplace transform of Equation (8), Equation (9) can be obtained as:

$$\frac{I_q(s)}{U_q(s) - K_u \omega_r(s)} = \frac{1}{R_s + L_q \cdot s} \tag{9}$$

where $P_n \psi_f = K_u$.

According to the electromagnetic torque equation for the PMSM (Equations (2)–(9)), the servo control strategy adopts a P-PI cascade controller to decrease disturbance attenuation and improve the control performance of the PMSM.

Figure 5 shows the control block diagram of the P-PI cascade controller for the DBSFDS. K_{ip}, K_{vp}, and K_{pp} denote the feedback coefficients of current loop, velocity loop, and position loop, respectively. The system includes two P-PI cascade controller structures with two P-position controllers, G_{X1P} and G_{X2P}, and two PI-velocity controllers, G_{X1V} and G_{X2V}. The expressions of G_{X1P}, G_{X2P}, G_{X1V}, and G_{X2V} are described in [44] and shown in Equation (10).

$$\begin{cases} G_{X1P} = K_{p1}, G_{X2P} = K_{p2} \\ G_{X1V} = K_{pv1} \frac{(T_{v1}s+1)}{T_{v1}s}, G_{X2V} = K_{pv2} \frac{(T_{v2}s+1)}{T_{v2}s} \end{cases} \tag{10}$$

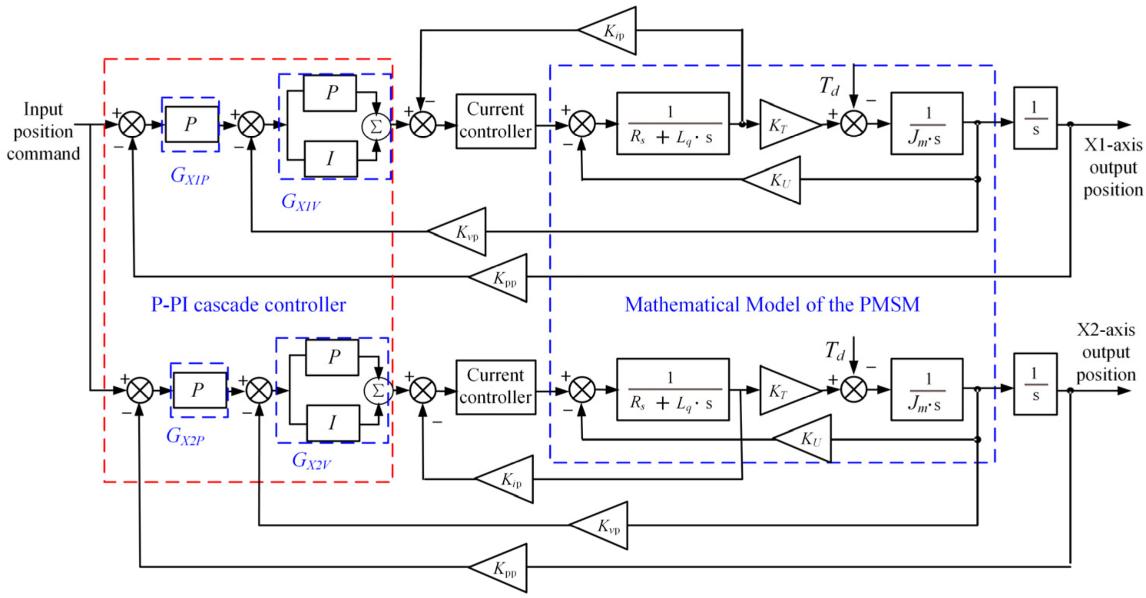

Figure 5. The control block diagram of the P-PI cascade controller for the DBSFDS.

3. Flexible Coupling Model for DBSFDSs

3.1. Coupling Mechanism of DBSFDSs

The dynamic characteristics of the DBSFDSs change owing to the flexibility of the ball-screw FDS and the variation in the position of the moving parts during movement. In addition, the flexible coupling of the two FDSs causes vibration and positioning errors in the X1-axis and X2-axis. All these factors reduce the motion accuracy of the tool center.

Figure 6 shows the flexible coupling model for DBSFDSs. Owing to non-synchronization errors, the DBSFDS exhibits linear motion along the X-direction and torsional motion around the Z-axis. The flexible coupling model of the DBSFDS is expressed in Equation (11) according to the Lagrange equation.

$$\begin{cases} m_c\ddot{x}_c = F_{d1} + F_{d2} - c\dot{x}_c \\ J_c\ddot{\theta}_c = F_{d1}l_1 - F_{d2}l_2 - k_\theta\theta_c \end{cases} \tag{11}$$

where m_c is the mass of the combination part (containing crossbeam and moving parts), and the expression is $m_c = m_1 + m_2$, where m_1 is the mass of the crossbeam, m_2 is the mass of the moving parts, and c is the damping of the combination part and is expressed as $c = c_{e1} + c_{e2}$. k_θ is the anti-torsional stiffness, and its value is related to the contact stiffness of the linear guide and the slider. J_c is the moment of inertia of the combination part around the center of gravity for the combination part o_c; x_c is the equivalent displacement of the combinatorial mass center; and F_{d1} and F_{d2} are the driving forces of the X1-axis and X2-axis, respectively. l_1 and l_2 indicate the distance from the o_c to the X1-axis and the distance from the o_c to the X2-axis, respectively, and their expressions are given in Equation (12).

$$\begin{cases} l_1 = \frac{l}{2} + \frac{m_2}{m_1+m_2}(y - \frac{l}{2}) \\ l_2 = l - l_1 \end{cases} \tag{12}$$

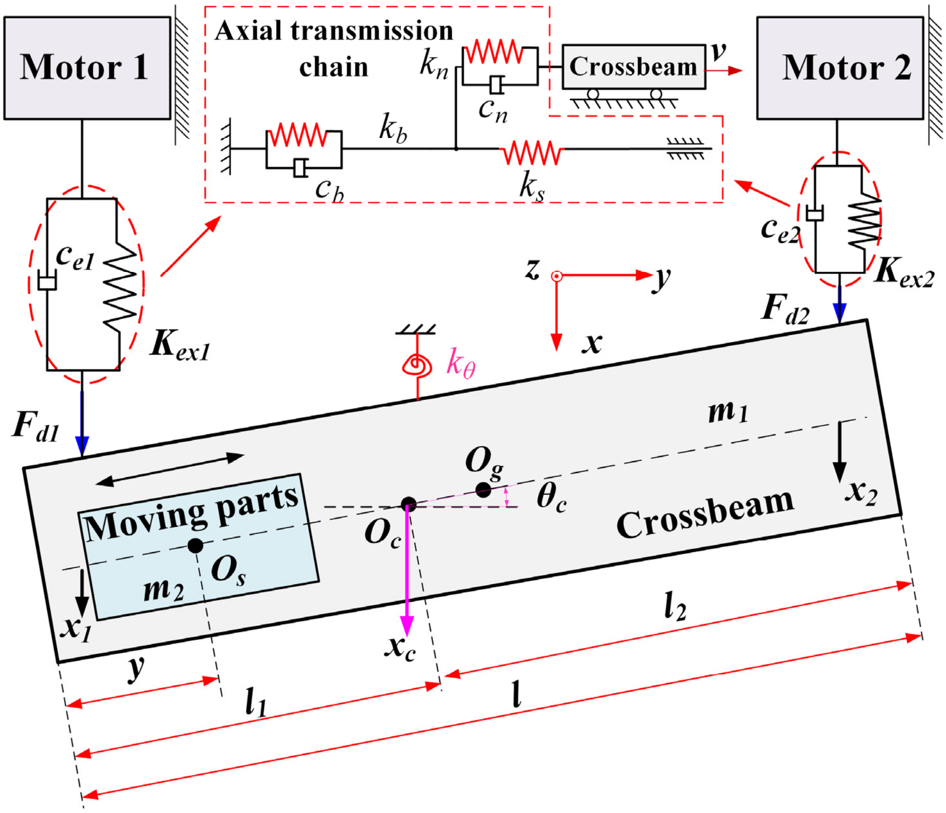

Figure 6. Flexible coupling model for DBSFDSs.

During machining, y changes in real time. The relationship among x_1, x_2, and x_c is given by Equation (13) based on the geometric–physical relationship.

$$\begin{bmatrix} x_1 \\ x_2 \end{bmatrix} = \begin{bmatrix} 1 & -l_1 \\ 1 & l_2 \end{bmatrix} \begin{bmatrix} x_c \\ \theta_c \end{bmatrix} \tag{13}$$

where x_1 and x_2 indicate equivalent displacement of the X1-axis and X2-axis.

The driving forces of the two FDSs can be obtained using Equation (14).

$$\begin{cases} F_{d1} = K_{ex1}(x_0 - x_1) \\ F_{d2} = K_{ex2}(x_0 - x_2) \end{cases} \tag{14}$$

where K_{ex1} and K_{ex2} denote the equivalent axial transmission stiffnesses of the X1-axis and X2-axis, respectively. The axial transmission stiffnesses are influenced by kinematic joints such as ball-screw and nut joints, ball bearings, and screw-shafts [45].

The relationship among J_c, J_g, and J_s can be expressed as:

$$\begin{cases} J_c = J_g + J_s \\ J_g = \frac{m_1 l^2}{12} + m_1 (l_1 - \frac{l}{2})^2 \\ J_s = m_2 (l_1 - y)^2 \end{cases} \tag{15}$$

where J_c is the moment of inertia of the crossbeam around the center of gravity for crossbeam o_c; and J_g and J_s are the moments of inertia of the crossbeam and moving parts around o_c, respectively.

Combining Equation (15) and the geometric parameter values, the relationship between the rotational inertia of the combination part and the position of the moving parts can be obtained, as shown in Figure 7. It can be observed that J_c has a minimum value when the moving parts are in the middle position (Position B). The range of change of J_c

was 47.15% over the course of the entire travel of the moving parts. Therefore, during the motion of the DBSFDS, the impact of the structural characteristic changes on the accuracy of the movement must be considered.

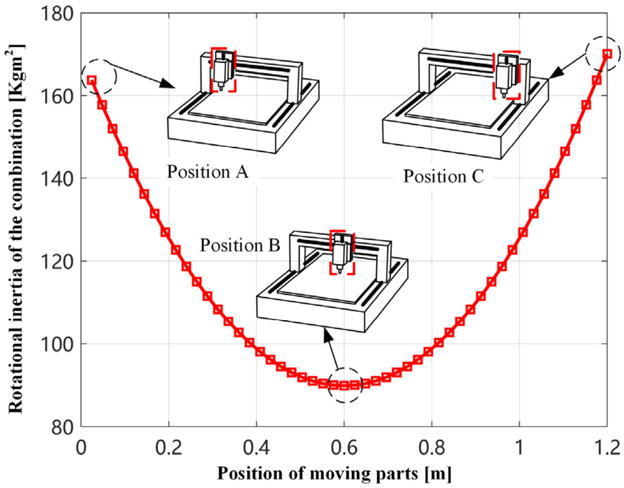

Figure 7. Variation of rotational inertia for the combination part.

According to Equation (11), the multiple-input and multiple-output systems of the DBSFDSs can be described as

$$\sum : \begin{cases} \dot{\boldsymbol{X}}(t) = \widetilde{\boldsymbol{A}} \times \boldsymbol{X}(t) + \widetilde{\boldsymbol{B}} \times \boldsymbol{U}(t) \\ \boldsymbol{Y}(t) = \widetilde{\boldsymbol{C}} \times \boldsymbol{X}(t) + \widetilde{\boldsymbol{D}} \times \boldsymbol{U}(t) \end{cases} \tag{16}$$

where $\widetilde{\boldsymbol{A}}$ is the system matrix, $\widetilde{\boldsymbol{B}}$ denotes the input matrix, $\widetilde{\boldsymbol{C}}$ represents the output matrix, $\widetilde{\boldsymbol{D}}$ is the transfer matrix, and $\boldsymbol{U}(t)$ is the control signal. Their expressions are $\boldsymbol{X}(t) = \begin{bmatrix} x_c & \theta_c & \dot{x}_c & \dot{\theta}_c \end{bmatrix}^T_{4\times 1}$, $\boldsymbol{U}(t) = \begin{bmatrix} F_{d1} & F_{d2} \end{bmatrix}^T_{2\times 1}$, and $\boldsymbol{Y}(t) = \begin{bmatrix} x_1 & x_2 \end{bmatrix}^T_{2\times 1}$
$\widetilde{\boldsymbol{A}} = \begin{bmatrix} 0 & 0 & 1 & 0 \\ 0 & 0 & 0 & 1 \\ 0 & 0 & -\frac{c}{m_c} & 0 \\ 0 & -\frac{k_\theta}{J_c} & 0 & 0 \end{bmatrix}_{4\times 4}$, $\widetilde{\boldsymbol{B}} = \begin{bmatrix} 0 & 0 \\ 0 & 0 \\ \frac{1}{m_c} & \frac{1}{m_c} \\ \frac{l_1}{J_c} & -\frac{l_2}{J_c} \end{bmatrix}_{4\times 2}$, $\widetilde{\boldsymbol{C}} = \begin{bmatrix} 1 & -l_1 & 0 & 0 \\ 1 & l_2 & 0 & 0 \end{bmatrix}_{2\times 4}$, and $\widetilde{\boldsymbol{D}} = [\boldsymbol{0}]_{2\times 2}$.

According to Equation (16), the transfer function of the actual displacements of the X1-axis and X2-axis to the two-axis driving force can be expressed as follows:

$$\begin{aligned} G = \widetilde{\boldsymbol{C}}(\boldsymbol{I}s - \widetilde{\boldsymbol{A}})^{-1}\widetilde{\boldsymbol{B}} = \begin{bmatrix} G_{11} & G_{21} \\ G_{21} & G_{22} \end{bmatrix} = \frac{\begin{bmatrix} X_1 \\ X_2 \end{bmatrix}_{2\times 1}}{\begin{bmatrix} F_{d1} & F_{d2} \end{bmatrix}_{1\times 2}} \\ = \begin{bmatrix} \frac{1}{m_c s^2 + cs} - \frac{l_1^2}{J_c s^2 + k_\theta} & \frac{1}{m_c s^2 + cs} + \frac{l_1 l_2}{J_c s^2 + k_\theta} \\ \frac{1}{m_c s^2 + cs} + \frac{l_1 l_2}{J_c s^2 + k_\theta} & \frac{1}{m_c s^2 + cs} - \frac{l_2^2}{J_c s^2 + k_\theta} \end{bmatrix} \end{aligned} \tag{17}$$

where G_{11} and G_{22} represent the transfer functions from the two-axis driving force of the X1-axis and X2-axis to the actual displacements of the X1-axis and X2-axis ball screw, respectively. G_{12} and G_{21} are the transfer functions of the X1-axis and X2-axis, respectively.

Figure 8a,b show the bode plots of G_{11} and G_{22}, respectively. As shown in Figure 8a,b, the two-axis transfer function varies with the position of the moving part. G_{11} and G_{22} have the highest frequencies when the moving part is in the middle position ($y = 0.6m$) and the smallest magnitudes, which means that the system is more stable in this position. When the moving part is in the middle position, the DBSFDSs conform to the DCG principle; thus, the system is the most stable.

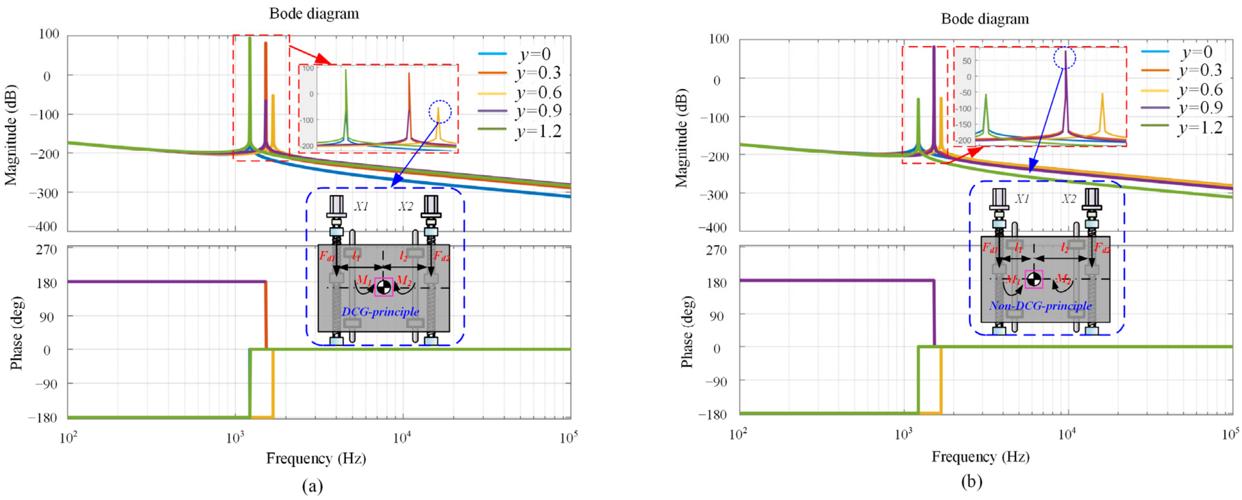

Figure 8. Bode plots of transfer functions (**a**) G_{11} and (**b**) G_{22}.

3.2. Flexible Model of DBSFDSs

To consider the influence of the elastic characteristics of the ball-screw FDS during P-PI cascade controller design, this study proposes the use of a motor current to identify the axial stiffness of DBSFDSs. Based on Equation (11), the flexible coupling model of the DBSFDS can be expressed as:

$$\boldsymbol{M}\ddot{\boldsymbol{x}} + \boldsymbol{C}\dot{\boldsymbol{x}} + \boldsymbol{K}\boldsymbol{x} = \boldsymbol{F} \tag{18}$$

matrices of the DBSFDS, respectively. $\dot{\boldsymbol{x}}$, $\ddot{\boldsymbol{x}}$, and $\ddot{\boldsymbol{x}}$ represent the vectors of displacement, velocity, and acceleration, respectively. $\boldsymbol{F}$ is a vector of the applied force applied to the DBSFDS.

Using the Fourier transform formula, Equation (18) can be written as:

$$\boldsymbol{X}(\omega) = \boldsymbol{G}(\omega)\boldsymbol{F}(\omega) \tag{19}$$

where $\boldsymbol{G}(\omega)$ is the frequency response function (FRF) of the DBSFDS, which can be expressed as Equation (20) [46].

$$\boldsymbol{G}(\omega) = \sum_{r=1}^{n} \left(\frac{\{L_r\}\{\phi_r\}^T}{j\omega - \lambda_r} + \frac{\{L_r{}^*\}\{\phi_r{}^*\}^H}{j\omega - \lambda_r^*} \right) \tag{20}$$

where the superscript T represents the transpose of a matrix; superscript * denotes the complex conjugate; n is the modal order of the system; and $\{\phi_r\}$ and $\{L_r\}$ are the r-th modal shape and modal participation factor, respectively. The superscript H represents a complex conjugate transpose operation, for example, Hermitian. λ_r is the r-th system pole. The expression λ_r can be written as:

$$\lambda_r, \lambda_r^* = -\xi_r\omega_r \pm j\sqrt{1 - \xi_r^2}\omega_r \tag{21}$$

where ξ_r and ω_r represent the damping ratio and natural frequencies, respectively.

According to the properties of the power spectral density (PSD) function, if the input signal meets the white noise condition, the self-power spectral density matrix of the response signal can be obtained as Equation (22).

$$\boldsymbol{G}_{ss}(\omega)=\underbrace{\sum_{r=1}^{n}\left(\frac{\{K_r\}\{\phi_r\}^T}{j\omega-\lambda_r}+\frac{\{K_r^*\}\{\phi_r^*\}^H}{j\omega-\lambda_r^*}\right)}_{\boldsymbol{G}_{ss}^{+}(\omega)}+\underbrace{\sum_{r=1}^{n}\left(\frac{\{K_r\}\{\phi_r\}^T}{-j\omega-\lambda_r}+\frac{\{K_r^*\}\{\phi_r^*\}^H}{-j\omega-\lambda_r^*}\right)}_{(\boldsymbol{G}_{ss}^{+}(\omega))^H} \tag{22}$$

where $\{K_r\}$ denotes the conditional reference factor. $\boldsymbol{G}_{ss}^{+}(\omega)$ represents the half-spectrum matrix of the PSD.

Equations (20) and (22) show that $\boldsymbol{G}_{ss}^{+}(\omega)$ and $\boldsymbol{G}(\omega)$ have similar forms. Hence, if the vibration excitation meets white noise conditions, the FRF can be replaced by the PSD. According to the theory of the FRF, the expressions of the function and modal admittance are described as

$$\begin{cases} H_{lp}(\omega)=\sum\limits_{r=1}^{N}\Phi_{lp}\Phi_{pr}H_r(\omega) \\ H_r(\omega)=\frac{1}{K_r'-\omega^2M_r+j\omega C_r}, r=1,2,\ldots,N \end{cases} \tag{23}$$

where $H_{lp}(\omega)$ is the FRF of the system; $H_r(\omega)$ is the r-th order modal admittance; and K_r', M_r, and C_r represent the modal stiffness, modal mass, and modal damping, respectively.

When the system is in resonance, $\omega \approx \omega_r$, and the following expression can be obtained.

$$\left|H_{lp}(\omega_r)\right| \approx \frac{1}{2\xi_r K_r'} \tag{24}$$

Thus, the system stiffness is

$$K_r'=\frac{1}{2\xi_r\left|H_{lp}(\omega_r)\right|} \tag{25}$$

where $\xi_r=\frac{C_r}{2M_r\omega_r}$ and $\omega_r{}^2=\frac{K_r'}{M_r}$.

To verify that the motor current can reflect axial vibration, an electromechanical simulation diagram of the DBSFDS can be derived based on the control block diagram of the PMSM (Figure 4). Table 3 lists the key parameters for the PMSM of the DBSFDS.

Table 3. Key parameters of the PMSM.

Parameters	Value/Units	Parameter	Value/Units	Parameter	Value/Units
Magnetic pole, P_n	10	Motor rotor inertia, J_m	48.2 kg·cm^2	Rated torque, T	11 N·m
Torque constant, K_r	1.63 N·m/A	Armature inductance, L_q	172 mH	Stator resistance, R_s	68 Ω

The simulation results in Figure 9b indicate that the axial vibration of the FDS can cause the motor output current to change. If a disturbance is introduced into the servo system, the motor current has the same component disturbance (the disturbance is indicated by the orange dotted line in Figure 9a). Furthermore, when sinusoidal periodic vibrations with a frequency of 125.6 rad/s (20 Hz) and frequency of 62.8 rad/s (10 Hz) were applied to the system in 3 s to 6 s, there were periodic fluctuations in the motor current, as shown in Figure 9a. The current spectrum shows that the current fluctuates and has the same frequency as the axial vibration. Therefore, the axial vibrations in the FDS are indicated by the motor current [47].

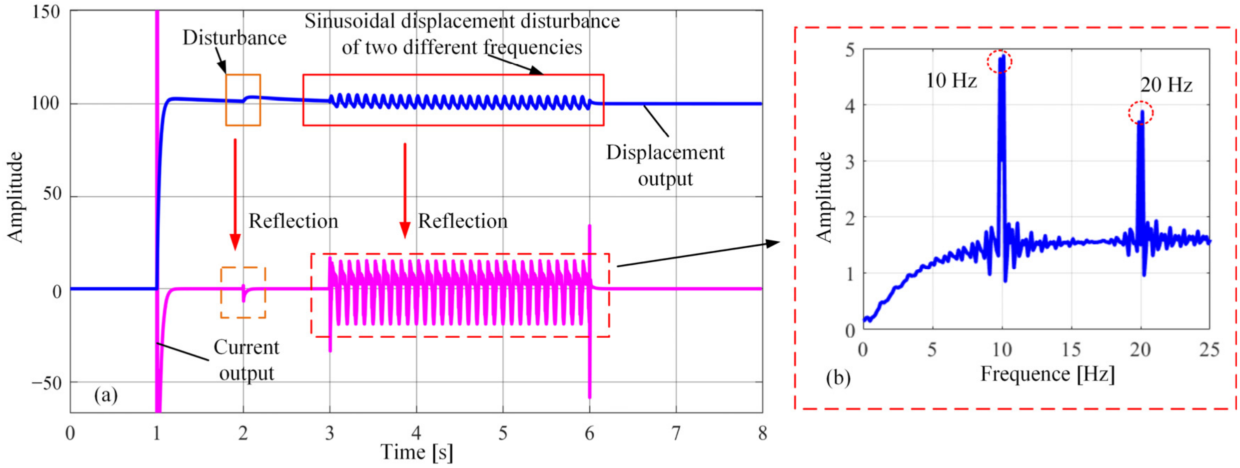

Figure 9. The simulation result of motor current remapping axial vibration. (**a**) The simulation result of the output current and (**b**) the axial vibration result.

Using the motor current (or motor torque) information to identify the axial stiffness of the DBSFDSs must ensure that the excitation satisfies the white noise characteristic. In particular, the inertial excitation vibration produced by the acceleration of the crossbeam must be random. The movement of the crossbeam can be programmed with suitable time intervals for the applied force to be considered random, which can achieve a certain bandwidth of white-noise excitation. Every inertial impact caused by the crossbeam acceleration and deceleration can be considered a pulse signal. Additionally, the impact time has white-noise characteristics. Therefore, the random acceleration and deceleration sequence can be regarded as a series of random pulse signals in the time domain [30].

The motor torque data of the axial stiffness identification experiment for the X1-axis are shown in Figure 10a,b. Figure 10a shows that the torque changes with motion. Moreover, the torque oscillated with an obvious overshoot after each starting cycle. This is because the axial vibration is fed back to the control system through the control of the PMSM, and the motor torque is adjusted accordingly. The motor torque data show that the fluctuation of the torque was affected by axial vibration. A vibration analysis program was used to analyze the PSD of the torque data. The PSD result is shown in Figure 10b. To obtain an exact identification result, the wavelet analysis method was used to reduce the influence of noise on the torque signal. There is a peak in Figure 10b, and the frequency of 97.7 Hz corresponds to the axial vibration of the DBSFDS. Combined with the equivalent mass of the DBSFDS, the identification result of the X1-axis axial transmission stiffness of the DBSFDSs was 101.84 N/μm. In addition, the axial transmission stiffness of the X2-axis was 100.52 N/μm.

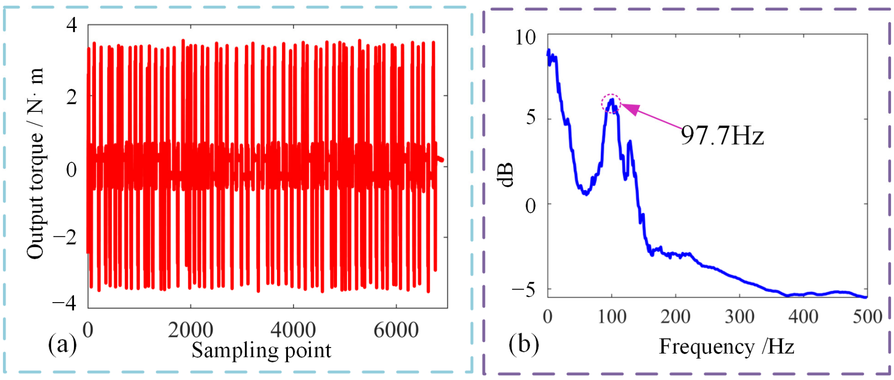

Figure 10. Stiffness identification results of the DBSFDS using the motor torque. (**a**) Output torque of PMSM. (**b**) PSD result of the output torque.

4. The Tuned P-PI Cascade Controller

4.1. GWO-Algorithm-Based Tuned P-PI Cascade Controller

From the above analysis, it can be seen that the position variation of the moving parts will affect the dynamic characteristics of the DBSFDS, and thus affect the motion accuracy. Therefore, the position variation of the moving parts should be considered when designing the control system of DBSFDSs. In a traditional P-PI cascade control, the PID parameters cannot change with the variation in the motion state, resulting in unsatisfactory motion control accuracy of the DBSFDS. Furthermore, in practice, it is difficult to simultaneously adjust the parameters of the X1-axis and X2-axis P-PI cascade controllers. Therefore, in view of the advantage of GWO [48], the GWO algorithm was used to adjust the PID parameters to adapt to the impact of the position variation of the moving parts on the control performance.

As shown in Figure 11, the P-PI cascade controller combined with the GWO algorithm is called the tuned P-PI cascade control of DBSFDSs. In industrial applications, the parameters of the current loop have been adjusted accurately, and the bandwidth of the current loop is much wider than those of the velocity and position loops; therefore, it can be assumed to be ideal. However, the parameters of the position and velocity loops must be adjusted. The GWO algorithm was used to adjust the parameters in the P-PI position-velocity cascade control. Specifically, it is necessary to adjust the X1-axis and X2-axis position loop gains K_{P1} and K_{P2}, velocity loop gains K_{Pv1} and K_{Pv2}, and integral time constants T_{v1} and T_{v2}. This is the first application example of GWO to adjust the P-PI cascade controller used for DBSFDSs for more accurate modeling.

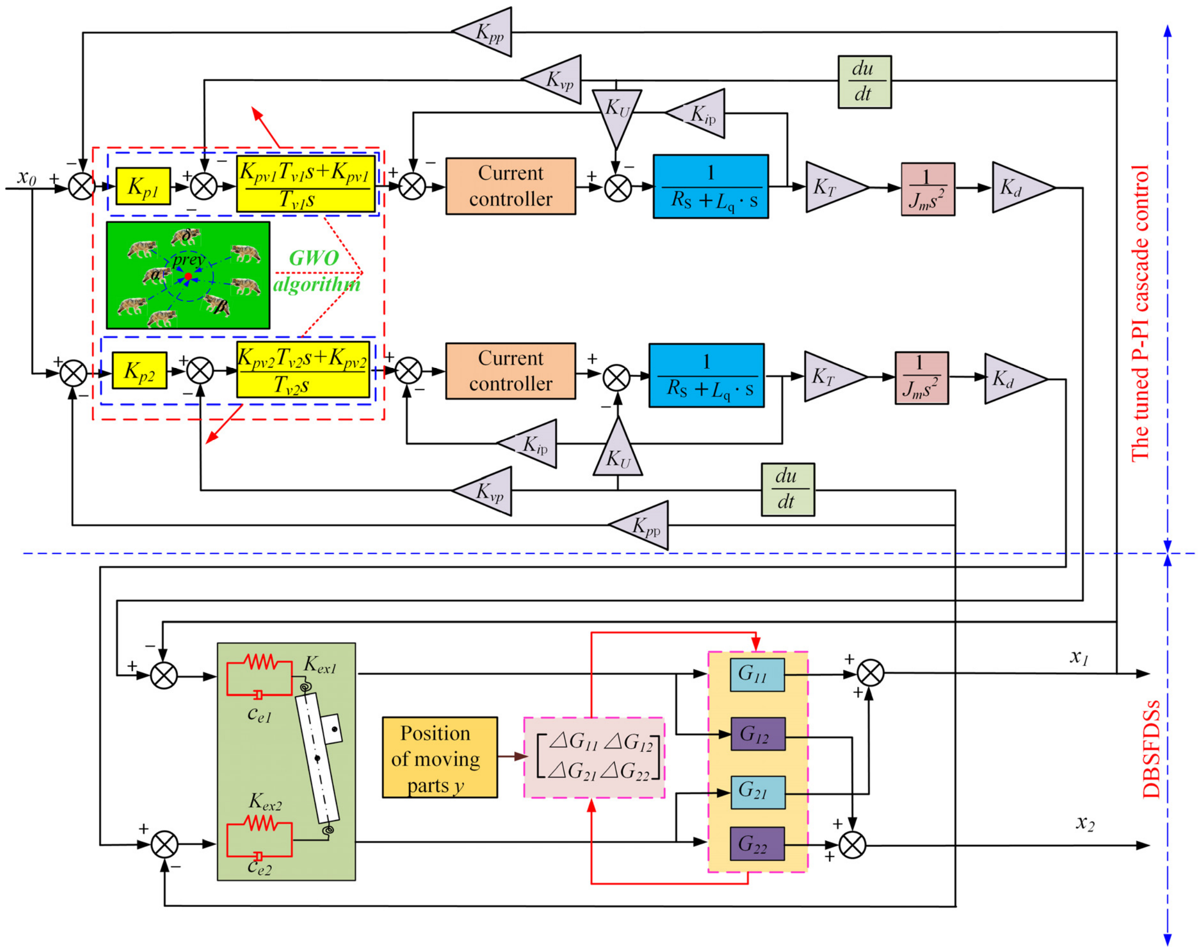

Figure 11. The structure diagram of the tuned P-PI cascade control.

The GWO algorithm is an intelligent algorithm based on the hunting mechanism of grey wolves. The prey represents the optimal solution, and the position of each grey wolf represents a potential solution. In the process of obtaining the optimal solution, grey wolves are sorted based on their fitness function values. Grey wolves with the best fitness function values are referred to as α wolves (leaders), followed by β wolves (second level), and δ wolves (third level), indicating that they are closest to the position of the prey. The remaining wolves are referred to as the ω wolves (lowest ranking). The grey wolf hierarchy plays an important role in predation, with α wolves leading the pack to surround the prey, β wolves and δ wolves attacking the prey, and ω wolves helping to attack the prey and eventually capture it [49]. The mathematical model of the GWO algorithm consists of track hunting, encircling prey, and attacking the prey.

$$\vec{D}_w = \left| \vec{C}_w \times \vec{X}_P(t) - \vec{X}(t) \right| \tag{26}$$

$$\vec{X}(t+1) = \vec{X}_P(t) - \vec{A}_w \times \vec{D}_w \tag{27}$$

Equations (26) and (27) represent the encircling behavior of grey wolves, where t indicates the current iteration, $\vec{A}_w$ and $\vec{C}_w$ are coefficient vectors, $\vec{X}_P(t)$ is the position vector of the prey, and $\vec{X}(t)$ refers to the position vector of the grey wolf. $\vec{A}_w$ and $\vec{C}_w$ are calculated as

$$\begin{cases} \vec{A}_w = 2\vec{a} \times \vec{r}_1 - \vec{a} \\ \vec{C}_w = 2 \times \vec{r}_2 \end{cases} \tag{28}$$

where $\vec{a}$ is the convergence factor, whose value decreases linearly from two to zero in the process. $\vec{r}_1$ and $\vec{r}_2$ are random vectors in [0, 1]. Equation (29) represents the track hunting of grey wolves.

$$\begin{cases} \vec{D}_\alpha = \left| \vec{C}_1 \times \vec{X}_\alpha - \vec{X} \right| \\ \vec{D}_\beta = \left| \vec{C}_2 \times \vec{X}_\beta - \vec{X} \right| \\ \vec{D}_\delta = \left| \vec{C}_3 \times \vec{X}_\delta - \vec{X} \right| \end{cases} \tag{29}$$

where $\vec{D}_\alpha$, $\vec{D}_\beta$, and $\vec{D}_\delta$ are the distances between α, β, δ, and the other individuals, respectively. $\vec{C}_1$, $\vec{C}_2$, and $\vec{C}_3$ are random vectors, and $\vec{X}$ is the current grey wolf position. The step length and direction of ω wolves toward α, β, and δ are shown by Equation (30), and Equation (31) represents the final position of the ω wolves.

$$\begin{cases} \vec{X}_1 = \vec{X}_\alpha - \vec{A}_1 \times (\vec{D}_\alpha) \\ \vec{X}_2 = \vec{X}_\beta - \vec{A}_2 \times (\vec{D}_\beta) \\ \vec{X}_3 = \vec{X}_\delta - \vec{A}_3 \times (\vec{D}_\delta) \end{cases} \tag{30}$$

$$\vec{X}(t+1) = \frac{\vec{X}_1 + \vec{X}_2 + \vec{X}_3}{3} \tag{31}$$

In the process of parameter adjustment of the P-PI controller, the fitness function affects the results of parameter tuning. Therefore, to ensure the overall performance of the control system, obtain satisfactory dynamic characteristics of the DBSFDSs, and consider the control accuracy and convergence speed, the integral time absolute error (ITAE) criterion [50] is chosen as the fitness function of the tuned P-PI cascade controller for DBSFDSs.

4.2. The Fitness Function Design Considering the Features of DBSFDSs

The design of the fitness function is a vital part of adjusting these parameters. Many studies considered only the dynamic response of a system. In this study, the dynamic response of the two axes and the dynamic characteristics of the two FDSs during the operation were considered simultaneously. As shown in Figure 12a, the rise time, overshoot, and steady-state error of DBSFDSs have been considered. However, the DBSFDSs will produce non-synchronous errors in the case of unequal tracking errors in the two FDSs, as shown in Figure 12b; therefore, the influence of the two-axis tracking error and the non-synchronization error should be considered in the fitness function. More importantly, the output torque of the two axes also consists of a fitness function to avoid excessive control energy. The empirical P-PI method cannot control the motor output torque during tuning.

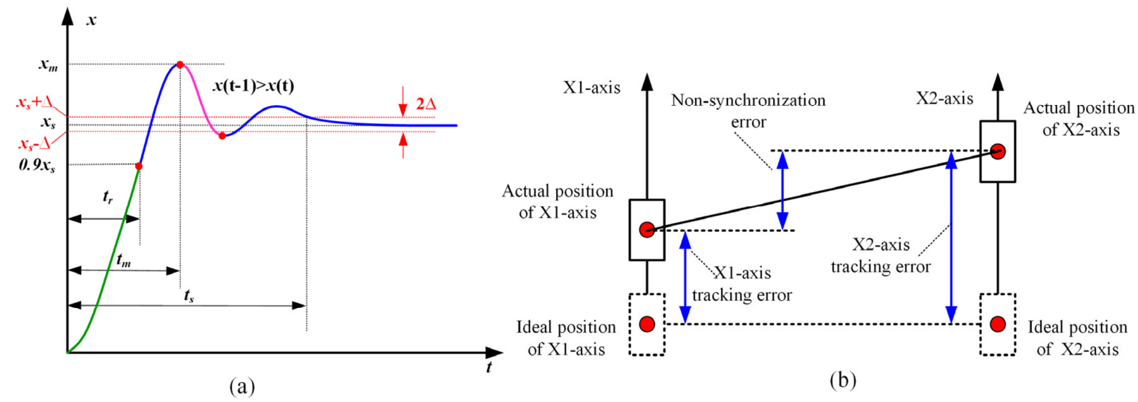

Figure 12. Dynamic response and non-synchronization error. (**a**) Indicators of dynamic response. (**b**) Tracking error and non-synchronous error of two FDSs.

Equation (32) is the expression of the fitness function of the DBSFDS; it contains the tracking errors of the two axes, the non-synchronization error, the output torques of the two axes, the overshoots of the two axes, and rising time.

$$J=\begin{cases}\int_0^T(\underbrace{\gamma_1 t|x_0(t)-x_1(t)|+\gamma_2 t|x_0(t)-x_2(t)|+\gamma_3 t|x_1(t)-x_2(t)|}_{\textit{Tracking error and non-synchronzation error}}+\\ \underbrace{\gamma_4 tF_1^2(t)+\gamma_5 tF_2^2(t)}_{\textit{Output torque}}+\underbrace{\gamma_6 t|F_1(t)-F_2(t)|}_{\substack{\textit{Difference of output torque}\\ \textit{between two axes}}})dt+\underbrace{\gamma_7 t_r}_{\textit{Rising time}}, & x(t-1)<x(t)\\ \int_0^T(\underbrace{\gamma_1 t|x_0(t)-x_1(t)|+\gamma_2 t|x_0(t)-x_2(t)|+\gamma_3 t|x_1(t)-x_2(t)|}_{\textit{Tracking error and non-synchronzation error}}\\ +\underbrace{\gamma_4 tF_1^2(t)+\gamma_5 tF_2^2(t)}_{\textit{Output torques}}+\underbrace{\gamma_6 t|F_1(t)-F_2(t)|}_{\substack{\textit{Difference of output torque}\\ \textit{between two axes}}}+\\ \underbrace{\gamma_8 t|x_1(t)-x_1(t-1)|+\gamma_9 t|x_2(t)-x_2(t-1)|}_{\textit{The overshoot of two axes}})dt+\underbrace{\gamma_7 t_r}_{\textit{Rising time}}, & x(t-1)>x(t)\end{cases} \tag{32}$$

where $x_0(t)$, $x_1(t)$, and $x_2(t)$ denote the reference signal, X1-axis displacement output, and X2-axis displacement output, respectively. $F_1(t)$ and $F_2(t)$ represent the output torques of the two FDSs, respectively. γ_1, γ_2, γ_3, γ_4, γ_5, γ_6, γ_7, γ_8, and γ_9 are the coefficients of the fitness function.

The setting of the parameters needs to be analyzed based on the coupling characteristics of the two axes of the DBSFDS. γ_1, γ_2, and γ_3 represent the coefficients of the X1-axis tracking error, X2-axis tracking error, and non-synchronization error, respectively. As shown in Figure 2, the expression for the non-synchronization error is $\Delta X_{sy} = \Delta X_{x1} - \Delta X_{x2} = |x_0 - x_1| - |x_0 - x_2|$. If the X1-axis and X2-axis tracking errors are equal to zero, the non-synchronization error drops to 0. However, if the non-synchronization error is zero, the errors of the two axes are not necessarily 0. Therefore, the values of γ_1 and γ_2 should be greater than that of γ_3. If an overshoot occurs in the system during the adjustment, that is, $x(t-1) > x(t)$, as indicated by the pink line in Figure 12a, the overshoots of the two axes are used as part of the fitness function. γ_8 and γ_9 are set as larger weighting coefficients to achieve a fast reduction in system overshoot. The rising time of the tool center is selected as part of the fitness function. It has the advantage of directly adjusting the rise time of the tool center by adjusting the PID parameters of the two axes, thus improving the tool-center response speed in actual motion.

On the other hand, many synchronization control methods for DBSFDSs mainly give priority to pure motion compensation and synchronization of the two axes. Even though the two axes have good motion accuracy, the dual actuator may still experience "pull-and-drag" phenomena through physical coupling between the X1-axis and X2-axis [51]. Therefore, if the difference between the output torques of the two FDSs is too large during operation, it causes the two FDSs to pull and drag each other and even destroy the DBSFDS. Therefore, γ_4, γ_5, and γ_6 are innovatively used to control the output torque and the difference in the output torques between the two actuators to reduce the influence of the non-synchronization error on the output torque of the two axes.

The process of tuning the P-PI cascade control of the DBSFDS is illustrated in Figure 13. The specific steps are as follows:

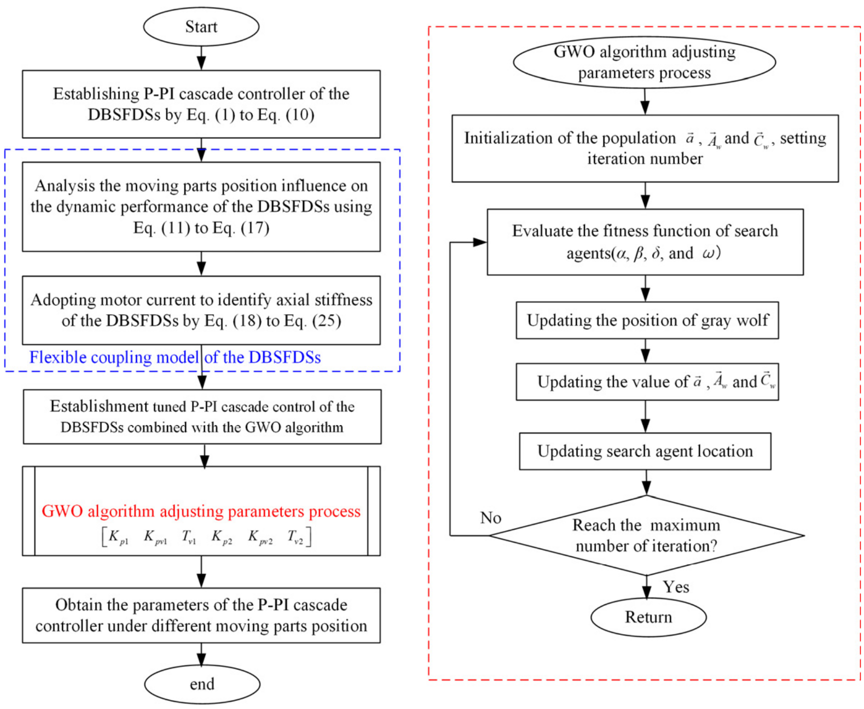

Figure 13. The flow chart of the tuned P-PI cascade control.

(1) Establish the simulation model of the DBSFDS and combine it with the GWO algorithm.
(2) Initialize the parameters of the GWO algorithm. The population size is set to 30, the dimension to 6, specifically $[K_{p1} \quad K_{pv1} \quad T_{v1} \quad K_{p2} \quad K_{pv2} \quad T_{v2}]$, the maximum number of iterations to 50, and the value range of each parameter is determined based on the experience value.

(3) Initialize the location information of the GWO algorithm. Calculate the corresponding fitness function value, and determine the global optimal position in the initialization phase.
(4) The algorithm is iterated until the termination condition is satisfied. The population is iterated according to Equations (26)–(32). Finally, the optimal parameter results are obtained.

According to the steps of the GWO algorithm, the parameter results of the tuned P-PI cascade controller at different positions of the moving parts can be obtained. According to the structural design of the DBSFDS, the travel of the moving parts is between 0 and 1.2 m. Tuning the P-PI parameters at the position y = 0, y = 0.3 m, y = 0.6 m, y = 0.9 m, and y = 1.2 m of the moving parts, the P-PI parameter adjustment results are taken as the P-PI controller value of the moving part position $y \in [0, 0.15)$, $y \in [0.15, 0.45)$, $y \in [0.45, 0.75)$, $y \in [0.75, 1.05)$, and $y \in [1.05, 1.2]$, respectively, to improve the adjustment efficiency. Figure 14a–c show the position-loop gain, velocity-loop gain, and integral time, respectively. It can be seen that, if a better control performance is achieved, the P-PI controller parameters will change as the position of the moving parts changes. In addition, the values of the P-PI parameters of the two axes exhibited different trends and changing ranges. During the entire stroke, the X1-axis and X2-axis position loop gains varied by 44.5% and 72.3%, respectively. The X1-axis and X2-axis velocity loop gains varied by 94.3% and 27.7%, respectively. The integral times of the X1-axis and X2-axis velocity loops varied by 139.9% and 63.4%, respectively. These results indicate that the position of the moving parts affects the variation in the PID parameters along the two axes.

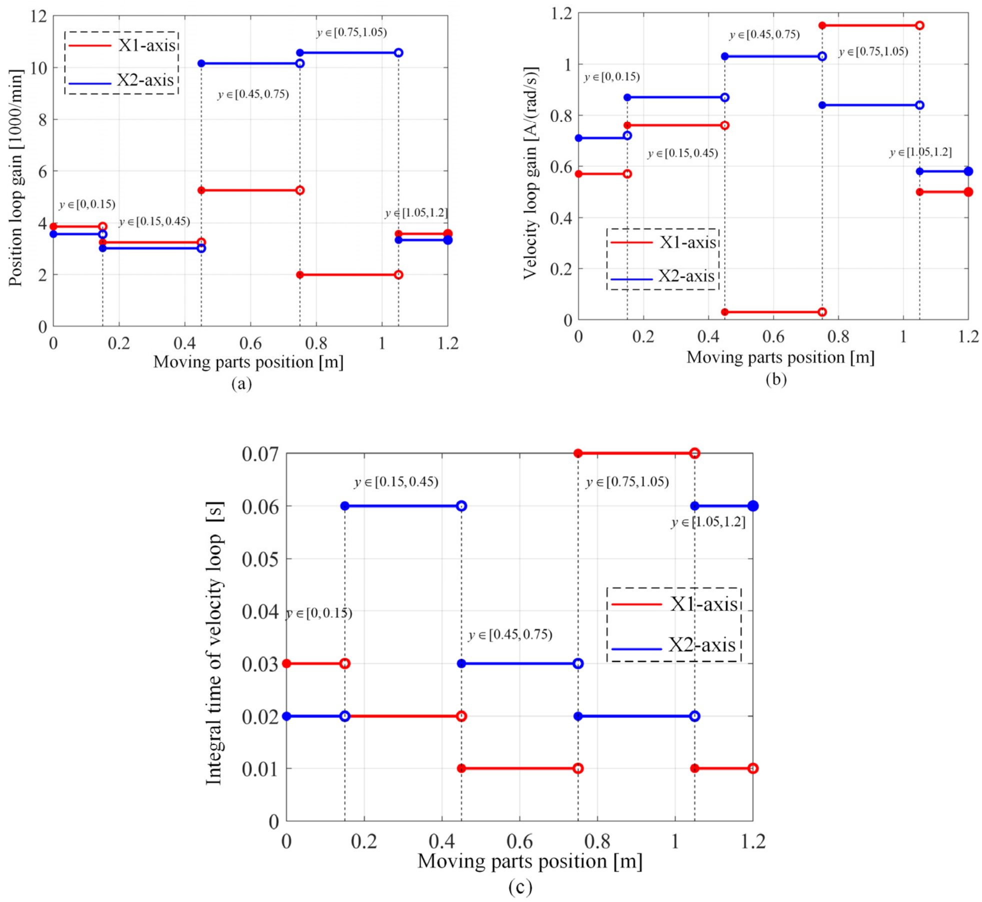

Figure 14. Parameter results of the tuned P-PI cascade control method. (**a**) The result of position-loop gain. (**b**) The result of velocity-loop gain. (**c**) The result of velocity-loop integral time.

5. Results and Discussion

5.1. Simulation

To verify the effectiveness of the tuned P-PI cascade control strategy proposed in this paper, an empirical method that uses the Ziegler–Nichols method to adjust the P-PI cascade control parameters (called the empirical P-PI control method) at different moving parts' positions and the proposed method were compared and analyzed. The empirical P-PI control method is a common and useful method for machine tool control; this has been proven by many researchers [52].

According to Equations (2)–(9), the control simulation model of the PMSM can be established. Based on Equations (11)–(17), a flexible coupling simulation model of DBSFDSs can be established. In addition, Equations (18)–(25) were used to identify the axial transmission stiffness of DBSFDSs. As described in the previous section, the transfer function of the mechanical system changes when the moving parts move along the crossbeam. A simulation was conducted to verify the effectiveness of the proposed control strategy. Real parameters of DBSFDSs were used in the simulation. The specifications are listed in Tables 3 and 4.

Table 4. Key parameters of the DBSFDSs.

Parameters	Value/Units	Parameters	Value/Units	Parameters	Value/Units
Rated power, P_r	3.46 kW	Rated speed, n	3000 r/min	Rated voltage, U	380 V
Rated current, I	7.8 A	The moving parts mass, m_1	317 Kg	The crossbeam mass, m_2	749 Kg
X1-axis axial stiffness, K_{ex1}	10.184×10^7 N/m	X2-axis axial stiffness, K_{ex2}	10.052×10^7 N/m	Anti-torsional stiffness, k_θ	9.8×10^9 N · m/rad

To prove that the proposed control method can effectively improve the feeding accuracy of the DBSFDSs, there are two aspects to verify during the simulation: (1) the response speed, overshoot, and control output torque of the proposed method and (2) the dynamic response and synchronization accuracy of the system under different input signals. The simulation results were compared with those obtained using the empirical P-PI control method under the same conditions.

5.1.1. Verification of the Response Speed, Control Output Torque, Tracking Error, and Non-Synchronization Error of the Proposed Method

To verify the effect of the tuned P-PI cascade control strategy, the moving parts are placed in different positions (y = 0.1 m, y = 0.4 m, y = 0.7 m, and y = 1.0 m). Figure 15a–d show the step response of the tool center, the output of the control torque, the tool center's tracking error, and the non-synchronization error of two control methods, respectively, under the condition of the moving parts' position y = 0.1 m. Simulations under other positions of the moving parts led to a similar conclusion. In Figure 15, the blue and red lines represent the results using the empirical P-PI control method and tuned P-PI cascade control method, respectively. In Figure 15a, using the tuned P-PI cascade control method, the rise time of the step response rise time was improved by 0.095 s, with no overshoot. In Figure 15b, adopting the method proposed in this study, the gain of the output force decreased by 10.60%, but the control effect improved, and the oscillation decay was accelerated by 0.0214 s, with a percentage of 3.98%. In Figure 15c,d, using the tuned P-PI cascade control method, the tracking error and non-synchronization error dropped faster than in the empirical P-PI control method, the tracking and synchronization errors reached 0, and the time was reduced by 0.1754 s and 0.1675 s, respectively. The percentages were 24.85% and 24.03%, respectively. Figure 15e shows that the maximum difference between the torques of the two axes can be reduced by 61.44% using the tuned P-PI cascade control method.

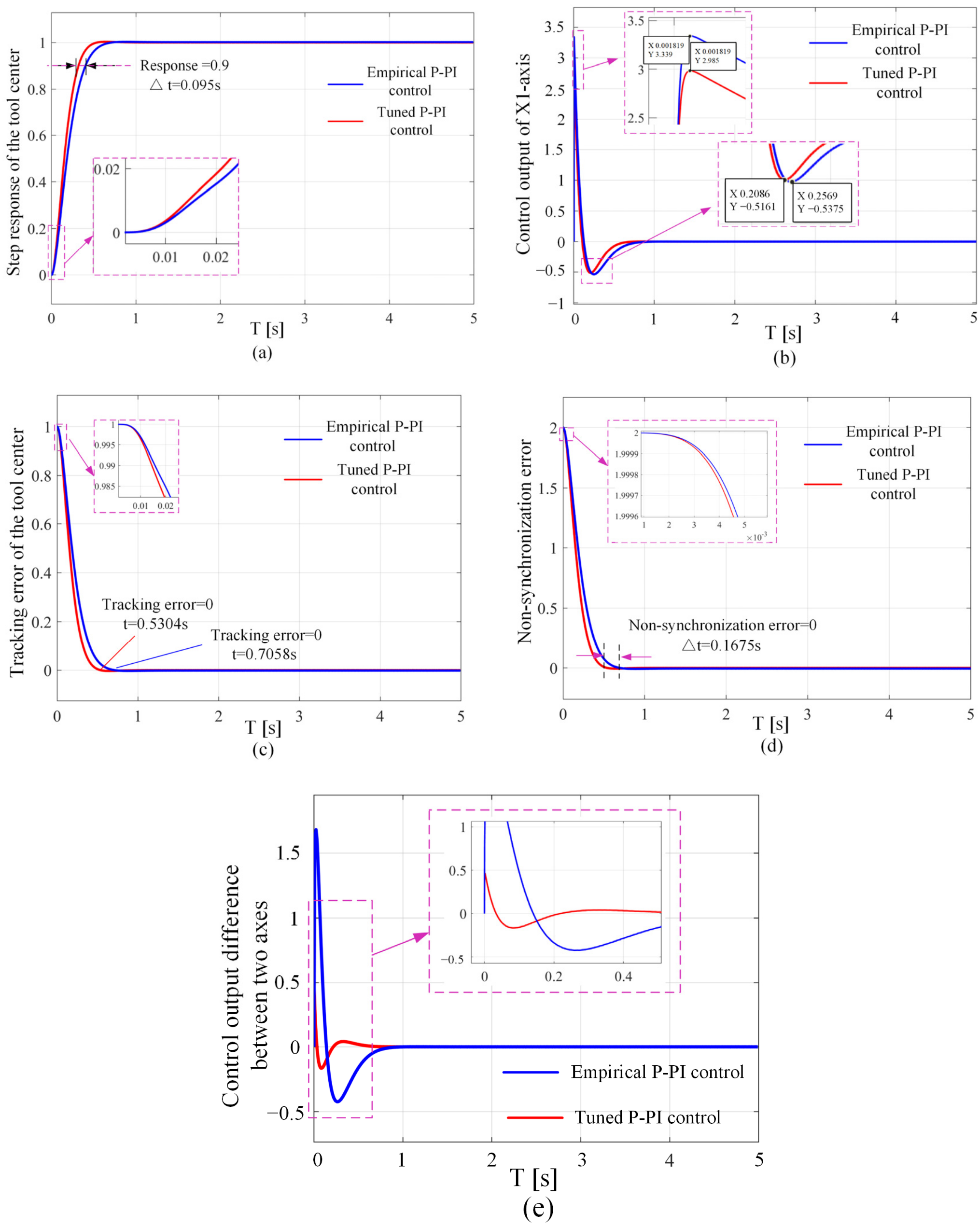

Figure 15. Comparison of the different control effects of the two methods. (**a**) Comparison results of the step response. (**b**) Comparison results of the control output. (**c**) Comparison results of the tracking error. (**d**) Comparison results of the non-synchronization error. (**e**) Comparison results of the control output difference.

The average error and the error standard deviation were used as evaluation criteria to assess the performance of the proposed control method in terms of the tracking accuracy of the tool center and dual-axis synchronization accuracy [53]. Their expressions are given in Equations (33) and (34), respectively.

$$\begin{cases} e_{tr}^{ave} = \sum\limits_{N=1}^{z} |e_{tr}(N)|/z \\ e_{tr}^{s} = \sqrt{\sum\limits_{N=1}^{z} (|e(N)| - e_{tr}^{ave})^2/z} \end{cases} \tag{33}$$

$$\begin{cases} e_{sy}^{ave} = \sum\limits_{N=1}^{z} \left| e_{sy}(N) \right| / z \\ e_{sy}^{s} = \sqrt{\sum\limits_{N=1}^{z} (|e(N)| - e_{sy}^{ave})^2 / z} \end{cases} \tag{34}$$

where e_{tr}^{ave} and e_{tr}^{s} represent the average tracking error and standard deviation of the tracking error, respectively. e_{sy}^{ave} and e_{sy}^{s} represents the average non-synchronization error and standard deviation of the non-synchronization error, respectively.

As shown in Table 5, the reduction in the average tracking error, average non-synchronization errors, standard deviation of the tracking error, and standard deviation of the non-synchronization error can reach 34.95, 34.03, 16.22, and 16.35%, respectively. Furthermore, in Table 6, the average output torque difference between the two axes and the standard deviation of the output torque difference between the two axes were reduced by 86.32 and 84.93%, respectively. The simulation results show that the tuned P-PI cascade method, response time, control output, tracking error, and non-synchronization error of the DBSFDS were better than those of the empirical P-PI control method. Tuned P-PI control can improve the tracking accuracy and synchronization accuracy of DBSFDSs. This is because the tuned P-PI cascade control method specifically considers the dynamic performance of the servo controller and the coupling characteristic between the X1-axis FDS and X2-axis FDS owing to the structural characteristic changes. More importantly, the tuned P-PI cascade control method focused on the output torque of the two actuators and reduced the difference in the output torque of the two axes. This is an absolute advantage over the other control methods. The GWO algorithm is used to adjust the P-PI parameters of the X1-axis and X2-axis simultaneously under different moving part positions, resulting in better performance.

Table 5. Simulation comparison of the two methods.

Comparison Items	Moving Parts' Position	Tuned P-PI Control	Empirical P-PI Control	Improvement
Average tracking error of the tool center	y = 0.1 m	0.034761	0.043659	20.38%
	y = 0.4 m	0.036458	0.048521	24.86%
	y = 0.7 m	0.036006	0.049055	26.60%
	y = 1.0 m	0.032265	0.049601	34.95%
Standard deviation of the tracking error	y = 0.1 m	0.146015	0.158980	8.16%
	y = 0.4 m	0.144155	0.164493	12.36%
	y = 0.7 m	0.144261	0.164279	12.19%
	y = 1.0 m	0.137454	0.164068	16.22%
Average non-synchronization error	y = 0.1 m	0.069525	0.088869	21.77%
	y = 0.4 m	0.072885	0.097747	25.44%
	y = 0.7 m	0.072016	0.097747	26.32%
	y = 1.0 m	0.064487	0.097747	34.03%
Standard deviation of the non-synchronization error	y = 0.1 m	0.292029	0.317396	7.99%
	y = 0.4 m	0.288302	0.328702	12.29%
	y = 0.7 m	0.288526	0.328700	12.22%
	y = 1.0 m	0.274957	0.328703	16.35%

Table 6. Simulation comparison of output torque difference for the two methods.

Comparison Items	Moving Parts' Position	Tuned P-PI Control	Empirical P-PI Control	Improvement
Average output torque difference between two axes	y = 0.1 m	0.007149	0.052259	86.32%
	y = 0.4 m	0.011988	0.061331	80.45%
	y = 0.7 m	0.011849	0.060929	80.55%
	y = 1.0 m	0.013471	0.060715	77.81%
Standard deviation of the output torque difference between two axes	y = 0.1 m	0.029294	0.194414	84.93%
	y = 0.4 m	0.048809	0.232756	79.03%
	y = 0.7 m	0.048931	0.232859	78.99%
	y = 1.0 m	0.049251	0.232915	78.85%

5.1.2. Verification of the Control Output and the Synchronization Accuracy of the System using Different Input Signals

The DBSFDSs continuously accelerate and decelerate during machining; therefore, different acceleration inputs are used to simulate the time-varying characteristics of the motion state. The dual-axis control output and positioning error were analyzed under different acceleration input conditions to verify the stability of the proposed control method.

Figure 16a shows the X1-axis output torque for the two control strategies with different velocity signal inputs when the moving part is at position y = 0.1 m. The tuned P-PI cascade control method had a lower output torque, faster response, and shorter adjustment time than the empirical P-PI control method. The dashed line box shows the input signals, the brown lines indicate the different velocity signals, and the green lines indicate the corresponding acceleration. The action time of the velocity is 4 s and can be expressed as

$$\begin{cases} e_{sy}^{ave} = \sum\limits_{N=1}^{z} \left| e_{sy}(N) \right| / z \\ e_{sy}^{s} = \sqrt{\sum\limits_{N=1}^{z} \left(|e(N)| - e_{sy}^{ave} \right)^2 / z} \end{cases} \tag{35}$$

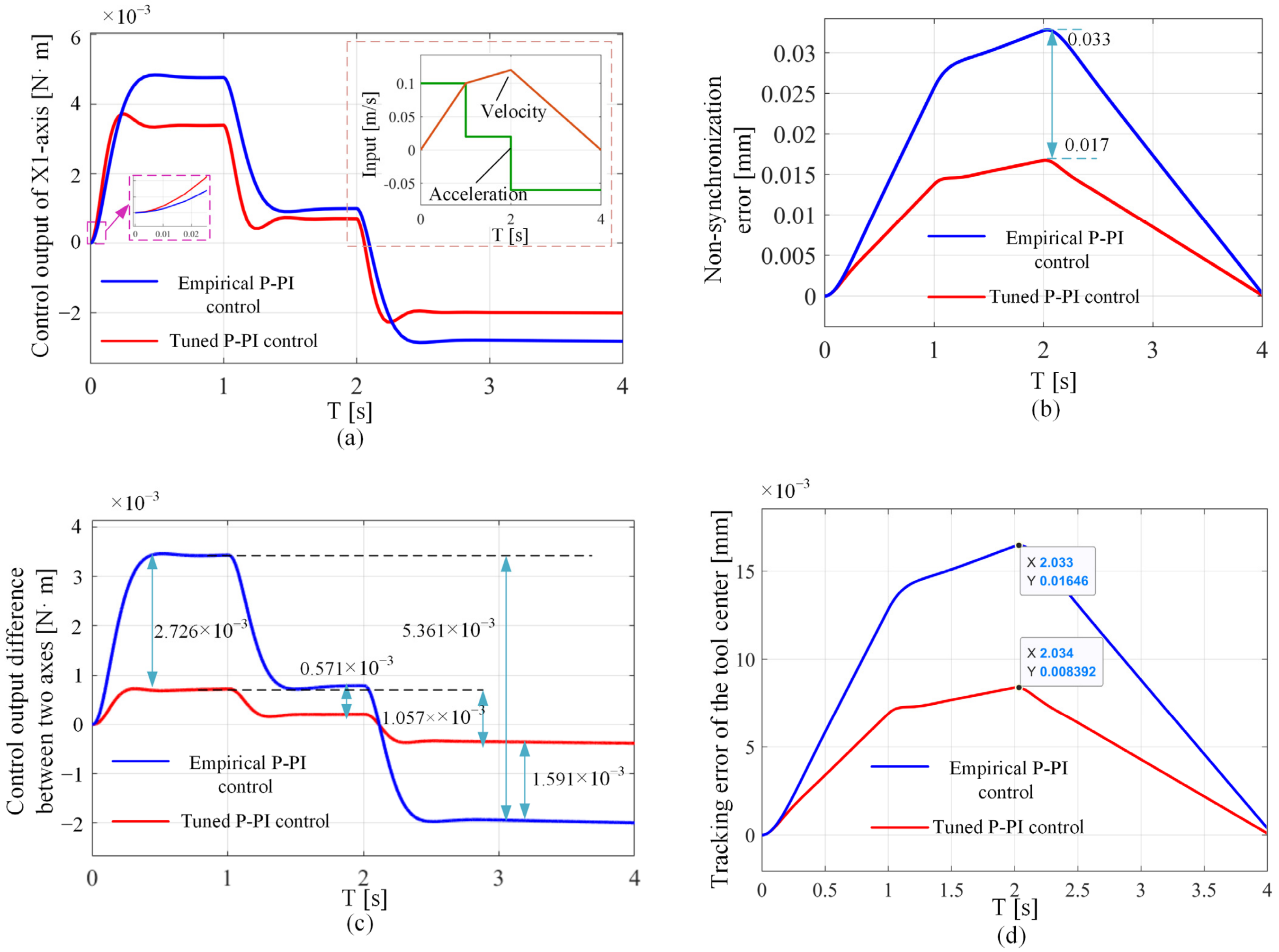

Figure 16. Control output and non-synchronization error of the two control methods. (**a**) Control output results. (**b**) Non-synchronization error results. (**c**) The results of control output difference. (**d**) Tracking error results.

Figure 16b shows the non-synchronization errors of the two control methods for different velocity signal inputs. It can be seen that the maximum non-synchronization error with the empirical P-PI control method was 0.033 mm, which is approximately twice as high as that with the tuned P-PI cascade control method. The average non-synchronization errors of the tuned P-PI cascade control method and empirical P-PI control method were 0.009786 and 0.019142, respectively. In addition, the standard deviations of the non-synchronization error for the tuned P-PI cascade control method and the empirical P-PI control method were 0.005221 and 0.010481, respectively. The simulation results for the other positions of the moving parts are listed in Table 7. Figure 16c shows the output difference between X1-axis and X2-axis. This shows that, compared to the empirical P-PI method, the P-PI tuned control method can result in a smaller difference in torque output between the two axes, not only during uniform acceleration but also during sudden speed changes. In addition, the variation in the difference between the output torques of the two axes during the entire motion was 19.72% of that of the empirical P-PI method. Figure 16d shows the variation in the tool-center tracking error when two control methods were used in the motion. The maximum tool-center tracking error using the tuned P-PI control method was 50.98% of that using the empirical method.

Table 7. Simulation comparison of different input signals.

Comparison Items	Moving Parts' Position	Tuned P-PI Control	Empirical P-PI Control	Improvement
Average non-synchronization error	y = 0.1 m	0.009786	0.019142	48.88%
	y = 0.4 m	0.024692	0.031621	21.91%
	y = 0.7 m	0.023873	0.032215	25.89%
	y = 1.0 m	0.021586	0.029848	27.68%
Standard deviation of the non-synchronization error	y = 0.1 m	0.005221	0.010481	50.19%
	y = 0.4 m	0.012986	0.018432	29.55%
	y = 0.7 m	0.012347	0.018774	34.23%
	y = 1.0 m	0.011428	0.016797	31.96%

From the two previously mentioned aspects of the simulation analysis, it can be observed that the tuned P-PI cascade control method has a good control effect on the position change of the moving parts. This method considers the load difference between the X1-axis and X2-axis caused by structural characteristic changes and adjusts the parameters of the two P-PI cascade controllers simultaneously, which can reflect the unification of the two FDSs during motion.

5.2. Experiments

The dual-drive gantry-type machine tool (DDGMT) used for the validation is shown in Figure 17. The crossbeam is driven by two ball screws with a 40 mm pitch, which are directly connected to two PMSMs by elastomer coupling. The DDGMT servo system employs a controller from the BECKHOFF company, in which the I/O module adopts the EtherCAT bus terminal module, which can make communication faster, simpler, and more cost-effective, and the control program was built using TwinCAT3® software [54].

To verify the effect of the tuned P-PI cascade control strategy, the moving parts were located at different positions (i.e., y = 0.1 m, y = 0.4 m) on the crossbeam when the crossbeam was in reciprocation motion. The feed speed of the crossbeam was set to 3000 mm/min, and the tracking error of the tool center and non-synchronization error were observed using optical scales. The sampling frequency and time were set to 500 Hz and 8 s, respectively. The maximum error, average error, and error standard deviation were adopted to evaluate the validity of the two methods, and their expressions are shown in Equations (33) and (34), respectively.

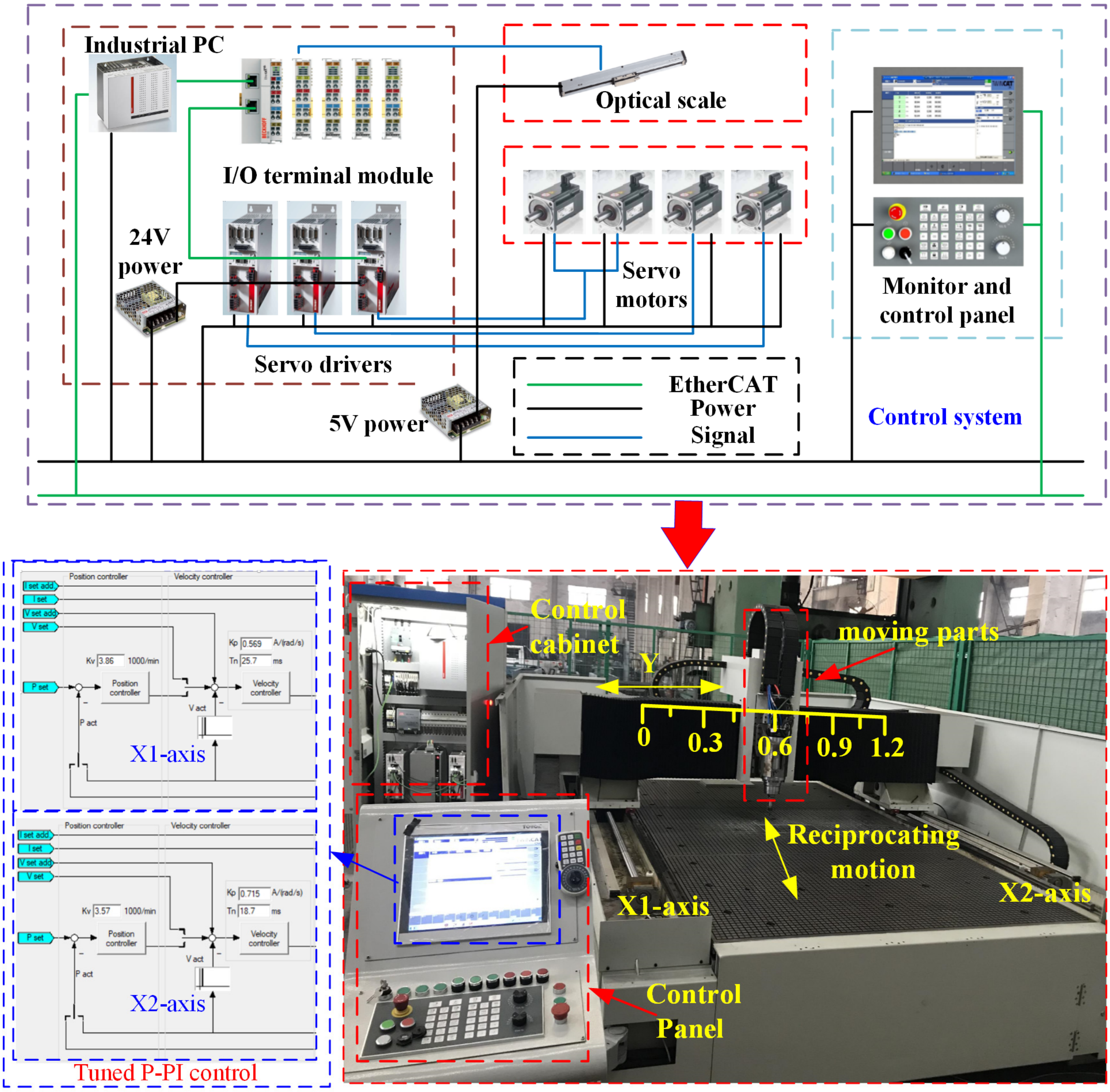

Figure 17. Control system of the DDGMT and experimental setup.

Figure 18 shows a typical experimental result. It can be seen that when the DDGMT starts and reverses, under the condition of moving parts' position y = 0.1 m, the peak values of the tracking errors and the non-synchronization errors of empirical P-PI control were 147.51 µm and 85.74 µm, respectively. The ranges of the tracking errors and non-synchronization errors were [−43 µm, 44 µm] and [−40 µm, 39 µm], respectively, when the system was in constant-speed operation. When the tuned P-PI control was implemented, the peak values of the tracking error and the non-synchronization error were 83.39 µm and 69.60 µm, respectively, in the events of starting and reversing. The ranges of the tracking errors and non-synchronization errors were [−30 µm, 33 µm] and [−16 µm, 16 µm], respectively, when the system was in constant-speed operation.

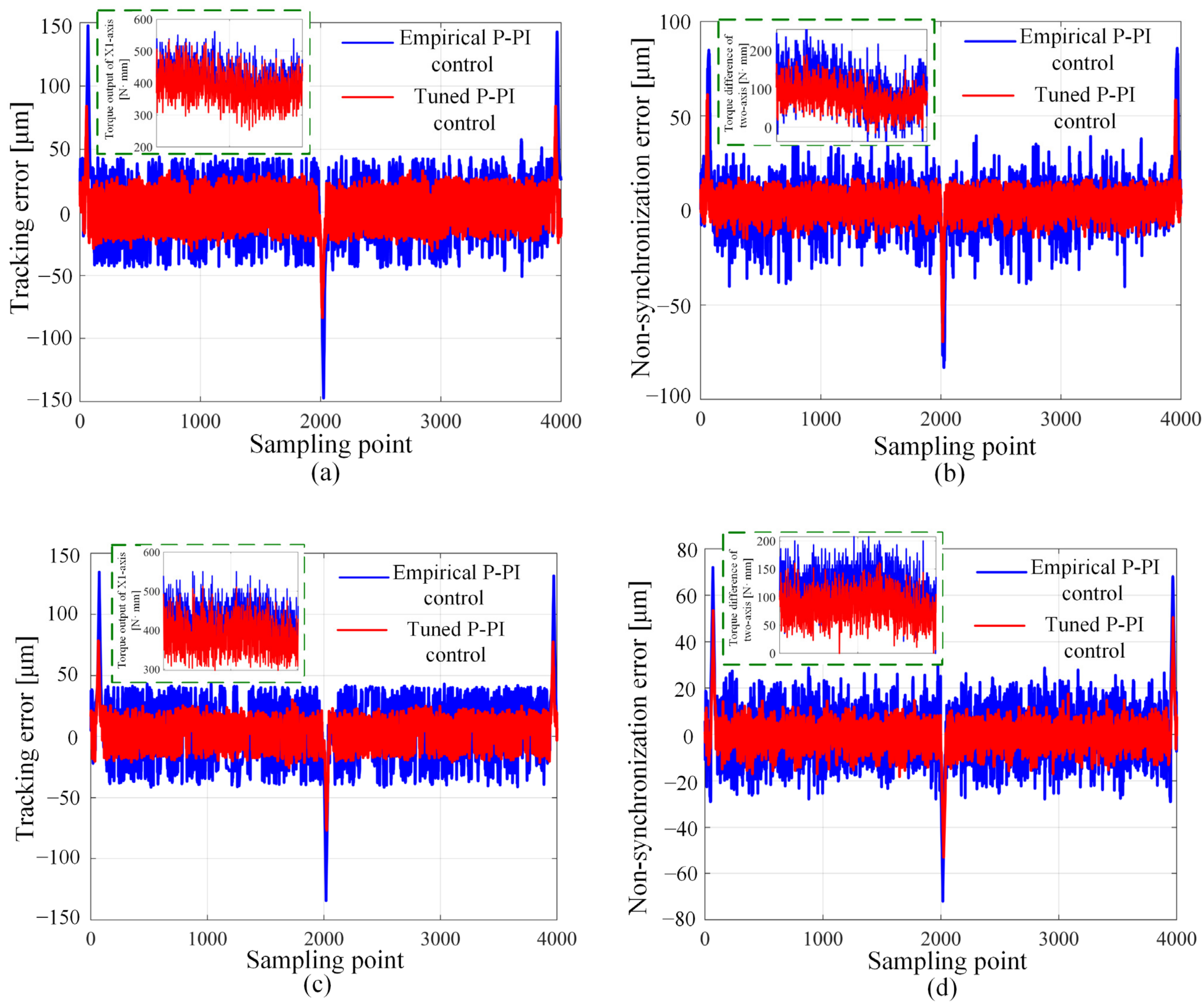

Figure 18. Comparison of experimental results of tuned P-PI control and empirical P-PI control. (**a**) Tracking error and (**b**) non-synchronization error comparison when y = 0.1 m; (**c**) tracking error and (**d**) non-synchronization error comparison when y = 0.4 m.

The green dashed boxes in Figure 18a,c indicate the torque output of the X1-axis in uniform motion for y = 0.1 m and 0.4 m, respectively. The green dashed boxes in Figure 18b,d indicate the torque difference of the X1-axis and X2-axis for y = 0.1 m and 0.4 m, respectively. As shown in Figure 18, with the tuned P-PI control, the gain of the torque output was smaller, and the fluctuation of the torque output was reduced. Furthermore, the difference in torque output between the two axes was smaller. The difference in torque between the two axes is due to the difference in friction between the two FDSs and motion non-synchronization errors. Table 8 shows the error standard deviation of the output torque difference between the X1-axis and X2-axis under different moving part positions. It can be seen that the tuned P-PI cascade control can effectively control the output torque of the two axes and reduce the difference between the torques of the two motors at each moving part position.

Table 8. Comparison of the experimental results of output torque difference.

	y = 0.1 m	**y = 0.4 m**	**y = 0.7 m**	**y = 1.0 m**
Empirical P-PI control	52.35	35.76	34.21	38.65
Tuned P-PI control	33.69	27.88	25.79	29.73
Improvement	35.64%	22.04%	24.60%	23.08%

In the same way, the experimental comparison of the empirical P-PI control and tuned P-PI control when y = 0.4 m can be obtained (shown in Figure 18c,d). The experimental results of different positions of the moving parts are summarized in Table 9. In Table 9, $\|e_{tr}\|_\infty = \max_t\{|e_{tr}|\}$ and $\|e_{sy}\|_\infty = \max_t\{|e_{sy}|\}$ represent the maximum tracking error and maximum non-synchronization error, respectively, as an index for the transient performance of the DDGMT [55]. According to the simulation and experimental results, it can be seen that using the GWO algorithm to adjust the parameters of the P-PI cascade controller can reduce the impact of the structural characteristic changes on the tool-center error and non-synchronization error of the two FDSs, thus improving the motion accuracy. Furthermore, compared to PSO, GWO calculates faster and requires less memory owing to one position vector. In addition, GWO maintains only the three best solutions, whereas PSO maintains the best solution for each particle, which limits the application of PSO according to reference [56].

Table 9. Comparison of experimental results for different positions of the moving parts.

Moving Parts' Position	Comparison	$\|e_{tr}\|_\infty$/µm	e_{tr}^{ave}/µm	e_{tr}^{s}/µm	$\|e_{sy}\|_\infty$/µm	e_{sy}^{ave}/µm	e_{sy}^{s}/µm
y = 0.1 m	Empirical P-PI control	147.51	22.22	26.93	85.74	10.05	14.56
	Tuned P-PI control	83.96	14.47	16.42	69.60	6.05	7.99
	Improvement	43.08%	34.86%	39.01%	18.83%	39.77%	45.11%
y = 0.4 m	Empirical P-PI control	134.47	22.95	26.49	72.03	8.99	12.41
	Tuned P-PI control	78.38	12.10	14.03	53.45	4.67	7.05
	Improvement	41.71%	47.28%	47.05%	25.79%	46.03%	43.19%
y = 0.7 m	Empirical P-PI control	131.27	22.88	14.41	77.14	11.23	10.14
	Tuned P-PI control	81.92	11.03	9.48	57.58	5.71	5.30
	Improvement	37.59%	51.79%	34.21%	25.36%	49.15%	47.73%
y = 1.0 m	Empirical P-PI control	142.57	26.16	16.52	83.58	12.55	11.43
	Tuned P-PI control	82.81	12.51	10.83	61.95	6.24	6.77
	Improvement	41.92%	52.18%	34.44%	25.88%	50.28%	40.77%

5.3. Discussion

According to simulation and experimental results, Tables 5–9 show the control effect of the grey-wolf-optimization-algorithm-based, tuned P-PI cascade controller. In the simulation experiments, the tool-center tracking error and the two-axis non-synchronization error, as well as the output torque difference were effectively reduced when the moving parts were in different positions with different input signals. In addition, the reduction in the standard deviation of the tracking error and the non-synchronization error indicates a reduction in the error fluctuations of the DBSFDS and furthermore an increase in the stability during operation.

In the experimental validation, compared to the empirical P-PI control method, when the moving parts were in different positions, the tuned P-PI control method could improve the reduction of average tracking error and standard deviation error of the tool center by 52.18% and 47.05%, respectively. For the reductions of the two-axis non-synchronization error of average error and standard deviation error were improved by 50.28% and 47.73%, respectively. The reduction in maximum tracking error and non-synchronization error indicate that the transient performance of the DDGMT was also improved during motion.

On the other hand, the experimental results verified the feasibility of the PID control method combined with the grey wolf optimization algorithm for the control of machine tools. The problem of mismatch between machine tool state changes and PID parameters can be solved. However, due to the limitations of the GWO algorithm such as premature convergence, future work is needed to improve the GWO algorithm such as the application of gaze-cues-learning-based grey wolf optimizer [39].

6. Conclusions and Future Work

The problems with using a P-PI cascade method to control DBSFDSs are (1) the mismatch between the dynamic performance and parameters of the P-PI cascade control method; (2) the parameters of two P-PI cascade controllers are always the same despite the two FDSs with different dynamic performances; and (3) it is hard to adjust two-axis PID parameters simultaneously. To handle these shortcomings, this paper presented a tuned P-PI cascade control for improving the accuracy of DBSFDSs, which can effectively decrease the feeding error of the tool center and non-synchronization errors. At the same time, this method can reduce the uneven output torque in the X1-axis and X2-axis owing to non-synchronization errors. Some useful scientific and technical conclusions are summarized below.

We established a flexible coupling model of DBSFDSs for tuning the parameters of the P-PI cascade controllers. The established flexible coupling model can describe the characteristics of two-axis coupling and reveal the mechanism of coupling two FDSs positioning errors with the tool-center error. Using motor current information to identify the axial stiffness of the DBSFDSs without any extra sensors is an easy and highly accurate method to acquire dynamic stiffness. This method solves the problem of not being able to obtain the dynamic stiffness of two axes simultaneously.

Based on the flexible coupling model, we created a tuned P-PI cascade control to improve the motion performance of DBSFDSs. The GWO algorithm was adopted to simultaneously adjust the parameters of the two P-PI cascade controllers to compensate for the characteristic variation. Tuned P-PI cascade control explicitly considers the difference in the parameters of the P-PI cascade controller owing to different loads on the two FDSs. The proposed control method was also compared with general tuning-based methods. Experimental and simulation results verified the effectiveness and superiority of the proposed tuned P-PI cascade controller in practical applications. The experimental results indicate that, in comparison with the conventional P-PI method, the proposed tuned P-PI cascade control can improve the position accuracy of the tool center to 34%. The proposed method provides a new approach for improving the feeding accuracy of DBSFDSs for practical industrial applications.

In future work, further improvement of the motion accuracy of the DBSFDSs will be made by improving the GWO algorithm and, in addition, using other high-quality metaheuristic algorithms via comparison experiments.

Author Contributions: Conceptualization, Q.L. and H.L.; methodology, H.Y., A.Y. and I.K.; software, Q.L. and B.W.; validation, Q.L. and H.L.; formal analysis, Q.L., H.Y. and I.K.; investigation, B.W.; resources, H.L.; data curation, Q.L. and B.W.; writing—original draft preparation, Q.L.; writing—review and editing, Q.L., H.L., H.Y., A.Y. and I.K.; supervision, H.L. and I.K.; project administration, I.K.; funding acquisition, Q.L. and H.L. All authors have read and agreed to the published version of the manuscript.

Funding: This research was funded by the National Natural Science Foundation of China [grant number 52275505] and the Chinese Government Scholarship by the China Scholarship Council [grand number 202106950009].

Data Availability Statement: Data sharing is not applicable to this article.

Conflicts of Interest: The authors declare no conflict of interest.

References

1. Xi, X.C.; Poo, A.N.; Hong, G.S. Improving Contouring Accuracy by Tuning Gains for a Bi-Axial CNC Machine. *Int. J. Mach. Tools Manuf.* **2009**, *49*, 395–406. [CrossRef]
2. Lin, M.T.; Wu, S.K. Modeling and Analysis of Servo Dynamics Errors on Measuring Paths of Five-Axis Machine Tools. *Int. J. Mach. Tools Manuf.* **2013**, *66*, 1–14. [CrossRef]
3. Hosseinkhani, Y. Control Methods for Improving Tracking Accuracy and Disturbance Rejection in Ball Screw Feed Drives. Ph.D. Thesis, University of Waterloo, Waterloo, ON, Canada, 2013.

4. Simba, K.R.; Bui, B.D.; Msukwa, M.R.; Uchiyama, N. Robust Iterative Learning Contouring Controller with Disturbance Observer for Machine Tool Feed Drives. *ISA Trans.* **2018**, *75*, 207–215. [CrossRef] [PubMed]
5. Yang, X.; Huang, M.; Wu, Y.; Feng, S. Observer-Based PID Control Protocol of Positive Multi-Agent Systems. *Mathematics* **2023**, *11*, 419. [CrossRef]
6. Miao, H.; Wang, C.; Li, C.; Song, W.; Zhang, X.; Xu, M. Nonlinear Dynamic Modeling and Vibration Analysis of Whole Machine Tool. *Int. J. Mech. Sci.* **2023**, *245*, 108122. [CrossRef]
7. Han, J.; Shan, X.; Liu, H.; Xiao, J.; Huang, T. Fuzzy Gain Scheduling PID Control of a Hybrid Robot Based on Dynamic Characteristics. *Mech. Mach. Theory* **2023**, *184*, 105283. [CrossRef]
8. Dong, L.; Tang, W.C. Adaptive Backstepping Sliding Mode Control of Flexible Ball Screw Drives with Time-Varying Parametric Uncertainties and Disturbances. *ISA Trans.* **2014**, *53*, 110–116. [CrossRef]
9. Hiramoto, K.; Hansel, A.; Ding, S.; Yamazaki, K. A Study on the Drive at Center of Gravity (DCG) Feed Principle and Its Application for Development of High Performance Machine Tool Systems. *CIRP Ann. Manuf. Technol.* **2005**, *54*, 333–336. [CrossRef]
10. Kamaldin, N.; Chen, S.L.; Teo, C.S.; Lin, W.; Tan, K.K. A Novel Adaptive Jerk Control with Application to Large Workspace Tracking on a Flexure-Linked Dual-Drive Gantry. *IEEE Trans. Ind. Electron.* **2019**, *66*, 5353–5363. [CrossRef]
11. Duan, M.; Lu, H.; Zhang, X.; Zhang, Y.; Li, Z.; Liu, Q. Dynamic Modeling and Experiment Research on Twin Ball Screw Feed System Considering the Joint Stiffness. *Symmetry* **2018**, *10*, 686. [CrossRef]
12. Teo, C.S.; Tan, K.K.; Lim, S.Y.; Huang, S.; Tay, E.B. Dynamic Modeling and Adaptive Control of a H-Type Gantry Stage. *Mechatronics* **2007**, *17*, 361–367. [CrossRef]
13. Yu, H.C.; Jang, C.S.; Peng, W.Y. Design Methodology and Self-Turning Velocity Control for High-Speed Slim Sensorless Brushless Direct Current Motors with Self-Lubricated Bearings. *Mech. Mach. Theory* **2015**, *84*, 134–144. [CrossRef]
14. Mudi, R.K.; Dey, C.; Lee, T.T. An Improved Auto-Tuning Scheme for PI Controllers. *ISA Trans.* **2008**, *47*, 45–52. [CrossRef] [PubMed]
15. Huba, M.; Vrancic, D. Tuning of PID Control for the Double Integrator Plus Dead Time Model by Modified Real Dominant Pole and Performance Portrait Methods. *Mathematics* **2022**, *10*, 971. [CrossRef]
16. Zhang, X.; Xu, X.; Xu, X.; Hou, P.; Gao, H.; Ma, F. Intelligent Adaptive PID Control for the Shaft Speed of a Marine Electric Propulsion System Based on the Evidential Reasoning Rule. *Mathematics* **2023**, *11*, 1145. [CrossRef]
17. Amiri, M.S.; Ramli, R. Utilisation of Initialised Observation Scheme for Multi-Joint Robotic Arm in Lyapunov-Based Adaptive Control Strategy. *Mathematics* **2022**, *10*, 3126. [CrossRef]
18. Haber-Haber, R.; Haber, R.; Schmittdiel, M.; del Toro, R.M. A Classic Solution for the Control of a High-Performance Drilling Process. *Int. J. Mach. Tools Manuf.* **2007**, *47*, 2290–2297. [CrossRef]
19. Ellis, G. *Control System Design Guide*, 4th ed.; China Machine Press-Publishing: Beijing, China, 2018.
20. Muresan, C.I.; De Keyser, R. Revisiting Ziegler–Nichols. *A fractional order approach. ISA Trans.* **2022**, *129*, 287–296.
21. Nadimi-Shahraki, M.H.; Taghian, S.; Mirjalili, S. An Improved Grey Wolf Optimizer for Solving Engineering Problems. *Expert Syst. Appl.* **2021**, *166*, 113917. [CrossRef]
22. He, Z.; Pan, B.; Liu, Z.; Tang, X. The Mechanical Arm Control Based on Harmony Search Genetic Algorithm. *Clust. Comput.* **2017**, *20*, 3251–3261. [CrossRef]
23. Sun, Z.; Ling, Y.; Qu, H.; Xiang, F.; Sun, Z.; Wu, F. An Adaptive DE Algorithm Based Fuzzy Logic Anti-Swing Controller for Overhead Crane Systems. *Int. J. Fuzzy Syst.* **2020**, *22*, 1905–1921. [CrossRef]
24. Jiang, M.; Wu, Y.; Jiang, L.; Li, F. Particle Swarm Optimization Algorithm Based on Natural Selection and Simulated Annealing for PID Controller Parameters. In *Simulation Tools and Techniques. SIMUtools 2019. Lecture Notes of the Institute for Computer Sciences, Social Informatics and Telecommunications Engineering*; Springer: Cham, Switzerland, 2019; pp. 363–373.
25. Faris, H.; Aljarah, I.; Al-Betar, M.A.; Mirjalili, S. Grey Wolf Optimizer: A Review of Recent Variants and Applications. *Neural Comput. Appl.* **2018**, *30*, 413–435. [CrossRef]
26. Zheng, Y.J. Water Wave Optimization: A New Nature-Inspired Metaheuristic. *Comput. Oper. Res.* **2015**, *55*, 1–11. [CrossRef]
27. Patel, V.K.; Savsani, V.J. Heat Transfer Search (HTS): A Novel Optimization Algorithm. *Inf. Sci.* **2015**, *324*, 217–246. [CrossRef]
28. Jee, S.; Koren, Y. Adaptive Fuzzy Logic Controller for Feed Drives of a CNC Machine Tool. *Mechatronics* **2004**, *14*, 299–326. [CrossRef]
29. Amiri, M.S.; Ramli, R.; Ibrahim, M.F.; Wahab, D.A.; Aliman, N. Adaptive Particle Swarm Optimization of Pid Gain Tuning for Lower-Limb Human Exoskeleton in Virtual Environment. *Mathematics* **2020**, *8*, 2040. [CrossRef]
30. Li, B.; Luo, B.; Mao, X.; Cai, H.; Peng, F.; Liu, H. A New Approach to Identifying the Dynamic Behavior of CNC Machine Tools with Respect to Different Worktable Feed Speeds. *Int. J. Mach. Tools Manuf.* **2013**, *72*, 73–84. [CrossRef]
31. Akbari, V.O.A.; Mohammadi, Y.; Kuffa, M.; Wegener, K. Identification of In-Process Machine Tool Dynamics Using Forced Vibrations in Milling Process. *Int. J. Mech. Sci.* **2023**, *239*, 107887. [CrossRef]
32. Xie, D.; Zhu, J.Q.; Wang, F. Fuzzy PID Control to Feed Servo System of CNC Machine Tool. *Procedia Eng.* **2012**, *29*, 2853–2858.
33. Gholap, V.; Dessai, C.N.; Bagyaveereswaran, V. PID Controller Tuning Using Metaheuristic Optimization Algorithms for Benchmark Problems. *IOP Conf. Ser. Mater. Sci. Eng.* **2017**, *263*, 052021. [CrossRef]
34. Yuan, Z.; Niu, M.Q.; Ma, H.; Gao, T.; Zang, J.; Zhang, Y.; Chen, L.Q. Predicting Mechanical Behaviors of Rubber Materials with Artificial Neural Networks. *Int. J. Mech. Sci.* **2023**, *249*, 108265. [CrossRef]

35. Das, K.R.; Das, D.; Das, J. Optimal Tuning of PID Controller Using GWO Algorithm for Speed Control in DC Motor. In Proceedings of the 2015 International Conference on Soft Computing Techniques and Implementations (ICSCTI), Faridabad, India, 8–10 October 2015; pp. 108–112.
36. Madadi, A.; Motlagh, M.M. Optimal control of dc motor using grey wolf optimizer algorithm. *TJEAS J.* **2014**, *4*, 373–379.
37. Wang, Y.; Jin, C.; Li, Q.; Hu, T.; Xu, Y.; Chen, C.; Zhang, Y.; Yang, Y. A Dynamic Opposite Learning-Assisted Grey Wolf Optimizer. *Symmetry* **2022**, *14*, 1871. [CrossRef]
38. Meidani, K.; Hemmasian, A.; Mirjalili, S.; Barati Farimani, A. Adaptive grey wolf optimizer. *Neural Comput. Appl.* **2022**, *34*, 7711–7731. [CrossRef]
39. Nadimi-Shahraki, M.H.; Taghian, S.; Mirjalili, S.; Zamani, H.; Bahreininejad, A. GGWO: Gaze cues learning-based grey wolf optimizer and its applications for solving engineering problems. *J. Comput. Sci.* **2022**, *61*, 101636. [CrossRef]
40. García-Herreros, I.; Kestelyn, X.; Gomand, J.; Coleman, R.; Barre, P.J. Model-Based Decoupling Control Method for Dual-Drive Gantry Stages: A Case Study with Experimental Validations. *Control Eng. Pract.* **2013**, *21*, 298–307. [CrossRef]
41. Zhen, N.; An, Q. Analysis of Stress and Fatigue Life of Ball Screw with Considering the Dimension Errors of Balls. *Int. J. Mech. Sci.* **2018**, *137*, 68–76. [CrossRef]
42. Neubauer, M.; Brenner, F.; Hinze, C.; Verl, A. Cascaded Sliding Mode Position Control (SMC-PI) for an Improved Dynamic Behavior of Elastic Feed Drives. *Int. J. Mach. Tools Manuf.* **2021**, *169*, 103796. [CrossRef]
43. Hu, M.; Ahn, H.; Chung, Y.; You, K. Speed Regulation for PMSM with Super-Twisting Sliding-Mode Controller via Disturbance Observer. *Mathematics* **2023**, *11*, 1618. [CrossRef]
44. Zhao, D.; Du, H.; Wang, H.; Zhu, Z. Development of a Novel Fast Tool Servo Using Topology Optimization. *Int. J. Mech. Sci.* **2023**, *250*, 108283. [CrossRef]
45. Mei, Z.; Ding, J.; Chen, L.; Pi, T.; Mei, Z. Hybrid Multi-Domain Analytical and Data-Driven Modeling for Feed Systems in Machine Tools. *Symmetry* **2019**, *11*, 1156. [CrossRef]
46. Liu, J.; Kizaki, T.; Ren, Z.; Sugita, N. Mode Shape Database-Based Estimation for Machine Tool Dynamics. *Int. J. Mech. Sci.* **2022**, *236*, 107739. [CrossRef]
47. Liu, X.; Mao, X.; Liu, H.; Li, B.; Guan, C.; Zhang, Z.; Luo, B.; Peng, F. Method for Identifying Feed-Drive System Dynamic Properties Using a Motor Current. *Int. J. Mach. Tools Manuf.* **2016**, *110*, 92–99. [CrossRef]
48. Mirjalili, S.; Mirjalili, S.M.; Lewis, A. Grey Wolf Optimizer. *Adv. Eng. Softw.* **2014**, *69*, 46–61. [CrossRef]
49. Bhatt, B.; Sharma, H.; Arora, K.; Joshi, G.P.; Shrestha, B. Levy Flight-Based Improved GreyWolf Optimization: A Solution for Various Engineering Problems. *Mathematics* **2023**, *11*, 1745. [CrossRef]
50. Abid, S.; El-Rifaie, A.M.; Elshahed, M.; Ginidi, A.R.; Shaheen, A.M.; Moustafa, G.; Tolba, M.A. Development of Slime Mold Optimizer with Application for Tuning Cascaded PD-PI Controller to Enhance Frequency Stability in Power Systems. *Mathematics* **2023**, *11*, 1796. [CrossRef]
51. Li, C.; Yao, B.; Wang, Q. Modeling and Synchronization Control of a Dual Drive Industrial Gantry Stage. *IEEE ASME Trans. Mechatron.* **2018**, *23*, 2940–2951. [CrossRef]
52. Sariyildiz, E.; Yu, H.; Ohnishi, K. A Practical Tuning Method for the Robust PID Controller with Velocity Feed-Back. *Machines* **2015**, *3*, 208–222. [CrossRef]
53. Mao, W.L.; Hung, C.W. Suprapto the Application of Proportional–Integral–Derivative–Type Fuzzy Controller for Synchronized XY Motion Gantry Stage System. *Adv. Mech. Eng.* **2018**, *10*, 1–15. [CrossRef]
54. Beckhoff. Beckhoff New Automation Technology. 2018. Available online: https://www.beckhoff.com.cn/english/ (accessed on 10 November 2018).
55. Li, C.; Li, C.; Chen, Z.; Yao, B. Advanced Synchronization Control of a Dual-Linear-Motor-Driven Gantry with Rotational Dynamics. *IEEE Trans. Ind. Electron.* **2018**, *65*, 7526–7535. [CrossRef]
56. Gad, A.G. Particle Swarm Optimization Algorithm and Its Applications: A Systematic Review. *Arch. Comput. Methods Eng.* **2022**, *29*, 2531–2561. [CrossRef]